

A critical Schrödinger cat qubit

Luca Gravina,^{1,2} Fabrizio Minganti,^{1,2} and Vincenzo Savona^{1,2,*}

¹*Institute of Physics, Ecole Polytechnique Fédérale de Lausanne (EPFL), CH-1015 Lausanne, Switzerland*

²*Center for Quantum Science and Engineering, Ecole Polytechnique Fédérale de Lausanne (EPFL), CH-1015 Lausanne, Switzerland*

(Dated: November 9, 2022)

Encoding quantum information onto bosonic systems is a promising route to quantum error correction. In a cat code, this encoding relies on the confinement of the system's dynamics onto the two-dimensional manifold spanned by Schrödinger cats of opposite parity. In *dissipative cat qubits*, an engineered dissipation scheme combining two-photon drive and two-photon dissipation has been used to autonomously stabilize this manifold, ensuring passive protection against, e.g., phase-flip errors regardless of their origin. Similarly, in *Kerr cat qubits*, where highly-performing gates can be engineered, two-photon drive and Kerr nonlinearity cooperate to confine the system to a two-fold degenerate ground state manifold spanned by cat states of opposite parity. To date, dissipative, Hamiltonian, and hybrid confinement mechanisms have been investigated at resonance, i.e., for driving frequencies matching that of the cavity. Here, we propose a *critical cat code*, where both two-photon dissipation and Kerr nonlinearity are present and the two-photon drive is allowed to be out of resonance. The competition between nonlinearity and detuning triggers a first-order dissipative phase transition, making the encoding efficient over a wide range of parameters in the proximity of the critical point. The performance of the code is benchmarked within the general framework of the Liouvillian spectral theory. We introduce a channel-fidelity decay rate, allowing for a fair comparison between our critical stabilization mechanism and its Hamiltonian, dissipative, and resonant-hybrid counterparts in the presence of both photon loss and dephasing noise. We find that the critical cat outperforms the others, and we show that this enhanced performance lies within reach of current experimental setups. Efficiently operating over a broad range of detuning values, the critical cat code is particularly resistant to random frequency shifts characterizing multiple-qubit operations, opening venues for the realization of reliable protocols for scalable and concatenated bosonic qubit architectures.

I. INTRODUCTION

The development of large-scale quantum computers relies on the possibility of taming errors, i.e., the irreversible processes stemming from the interaction of the system with its surrounding environment [1–4]. Quantum error correction schemes redundantly encode quantum information onto multi-level quantum systems, in a way that enables to detect and correct specific types of errors without affecting the stored quantum information [5–7]. The mainstream quantum error correction paradigm consists in encoding the $|0_L\rangle$ and $|1_L\rangle$ logical states onto a two-dimensional subspace of the Hilbert space characterizing the states of several physical qubits [1, 5]. Despite its promise of scalability, this type of encoding suffers from its large hardware footprint and the high connectivity between physical qubits required to execute fault-tolerant quantum computations.

An alternative paradigm to detect and correct quantum errors consists in encoding the logical states of a qubit onto an appropriately selected subspace of the Hilbert space of a harmonic oscillator [8–14]. These *bosonic quantum codes* are characterized by a reduced hardware footprint, and essentially eliminate the daunting challenge of simultaneously controlling the multiple

degrees of freedom of several physical qubits [15]. In these systems, information is encoded as a symmetric pattern in phase space [11]. While a translational symmetry underlies the GKP code [8], a rotational one characterizes the *Schrödinger cat code*, where the $|0_L\rangle$ and $|1_L\rangle$ logical states are mapped onto the cat states of opposite parity [9, 16].

Schrödinger cat qubits have been realized, in particular, on superconducting circuit platforms which are mainly prone to two noise processes: single particle loss and dephasing [11]. These directly map onto errors on the logical qubit, namely, bit- and phase-flip errors. Confinement of the system's dynamics to the cat manifold relies on a subtle interplay between engineered parametric processes. In recent years two approaches have been proposed to achieve this confinement.

Dissipative confinement relies on an engineered dissipation scheme combining two-photon drive G and two-photon dissipation η [9, 17–21] to generate and autonomously stabilize the code manifold. Dissipative cats are intrinsically resistant to “leakage” processes, ensuring an exponential suppression of the phase-flip error rate in the cat's photon number [9, 17, 22, 23]. Their main drawback is the limited performance of logical gates on current superconducting platforms [18, 24].

Hamiltonian confinement, on the other hand, relies on the Kerr nonlinearity U to restrict the system to the doubly degenerate ground space of the anharmonic oscillator [25–28]. Gate performance can be improved by the ap-

* vincenzo.savona@epfl.ch

plication of, e.g., super-adiabatic pulse designs [19], limiting the amount of leakage induced by gate operations. However, the Kerr nonlinearity amplifies the effect of dephasing, which is no longer exponentially suppressed in the cat's photon number [24].

Recently, a *hybrid* proposal [24], combining the two confinement protocols, has highlighted an unfavorable trade off between the stabilizing action of two-photon dissipation, and the Kerr-induced dephasing. It was shown that to retain a sizable exponential suppression of the logical phase-flip rate in the hybrid regime, the dissipative stabilization rate needs to dominate over the Kerr-induced dephasing – a constraint that severely limits the advantage brought by the combined confinement scheme [24]. In all these cases, the cat code remains vulnerable to bit-flip errors originating from photon loss processes. As such, cat qubits are the quintessential example of *biased-noise qubits* [11, 15].

Dissipative, Hamiltonian, and hybrid protocols alike all operate in a regime where the cavity is resonantly driven (the pump-to-cavity detuning is $\Delta = 0$). Only very recently, finite values of Δ have been explored, restricted to the limiting case of Hamiltonian confinement [29, 30]. Here, we adopt a novel perspective and operate the cat in a hybrid regime and in the presence of a sizable Δ . We dub our encoding a *critical cat code*. By exploring the parameter space, we prove that

- Efficient quantum information encoding is not limited to $\Delta = 0$ if $U \neq 0$, but extends over a broad range of values of Δ , where the qubit can be operated (Sec. III A).
- The presence of a dissipative phase transition (DPT) makes the qubit resilient against uncontrolled changes in its frequency (Sec. III C), that may originate for instance from the dispersive coupling to external reservoirs or ancillary circuitual elements [31]. The latter being typically required for the realization of two-qubit entangling gates or concatenated-qubit error-correction protocols.
- The critical cat *outperforms* its Hamiltonian, dissipative, and hybrid(-resonant) counterparts. To assess the improved performance, we introduce the channel-fidelity decay rate (Sec. II D), a measure of the loss of quantum information based on the spectrum of the Liouvillian superoperator, enabling direct comparison of different bosonic codes.
- Large photon numbers and *enhanced exponential suppression* of phase-flip errors can be achieved by simple detuning operations (Sec. IV). This is not the case for either the Hamiltonian or dissipative confinement schemes.

Intuitively, the enhanced performance of the critical cat originates from the introduction of detuning, which reduces the Kerr-induced amplification of dephasing noise [24, 26], making it possible to efficiently stabilize

the code manifold even with a moderate two-photon dissipation rate. On a more formal level, the advantage of this approach has roots in the emergence of a *first-order* DPT with spontaneous breaking of the system's strong \mathbb{Z}_2 symmetry [32]. DPTs have been the focus of intense theoretical and experimental research in recent years [33–47], having also been proposed as a resource for quantum metrology [48–51]. In particular, Ref. [31] demonstrated that quantum information could be encoded in the broken-symmetry phase of a *second order* DPT. We extend this idea to first-order DPTs with spontaneous symmetry breaking (SSB), and link the enhanced performance of the critical cat to the first-order criticality.

The article is structured as follows. In Sec. II we introduce the cat qubit and the dissipative/Hamiltonian processes underlying its generation. Upon performing an analysis of the Liouvillian superoperator, of its spectrum, and of its symmetries, we introduce the channel fidelity rate, a versatile quantifier of the decay of quantum information in bosonic codes in the presence of logical errors. In Section III, we unveil the *critical cat code* analyzing some of its properties under the lens of the spectral theory of Liouvillian superoperators. Here, we highlight the link between the symmetry properties of the Liouvillian, the ensuing first-order transition, and the structure of the steady-state manifold where quantum information is encoded. We further demonstrate the resistance of the critical cat against random frequency shifts. We then demonstrate the efficiency and robustness of the critical encoding. In Sec. IV we show the critical cat's enhanced suppression of the dephasing-induced phase-flip error rate, while Sec. V details the code's performance in the presence of both single-photon loss and dephasing. We draw our conclusions and discuss future perspectives in Sec. VI.

II. GENERATION AND STABILIZATION OF SCHRÖDINGER CATS

Schrödinger cat states are the even and odd superpositions of two coherent states of opposite phases

$$|\mathcal{C}_\alpha^\pm\rangle = \frac{|\alpha\rangle \pm |-\alpha\rangle}{2\sqrt{1 \pm e^{-2|\alpha|^2}}}, \quad (1)$$

where the coherent state $|\alpha\rangle$ is the eigenstate of the annihilation operator \hat{a} , i.e. $\hat{a}|\alpha\rangle = \alpha|\alpha\rangle$ [2, 52]. When expressed in the number (Fock) basis, $|\mathcal{C}_\alpha^\pm\rangle$ contain only components with respectively even and odd number of photons. As such, they are eigenstates of the parity operator $\hat{\Pi} = \exp(i\pi\hat{a}^\dagger\hat{a})$ with eigenvalues ± 1 . Their size (*cat size*) is defined as the average number of photons $\langle\hat{a}^\dagger\hat{a}\rangle = \text{Tr}(\hat{\rho}\hat{a}^\dagger\hat{a})$. In a Schrödinger cat code, the logical states of the qubit are encoded onto cats of opposite parity, namely $|\mathcal{C}_\alpha^+\rangle \equiv |0_L\rangle$ and $|\mathcal{C}_\alpha^-\rangle \equiv |1_L\rangle$ [c.f. Fig. 1 (a)] [53]. The generation and stabilization of Schrödinger cat codes heavily relies on processes involving exclusively the pairwise exchange of photons between the system and its

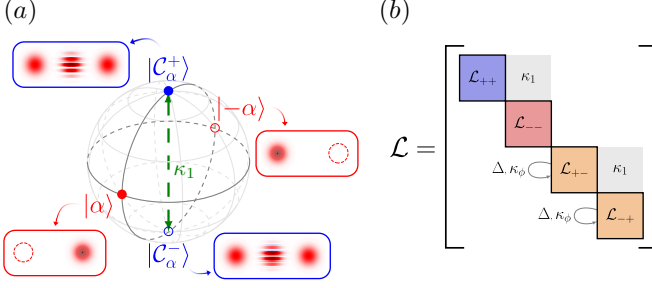


FIG. 1. (a) The even and odd cat states, represented by their Wigner functions, encode the logical states $|0_L\rangle$ and $|1_L\rangle$. Their superpositions, approximately the two coherent states $|\pm\alpha\rangle$, define the logical states $|\pm_L\rangle$. (c) Block structure of the Liouvillian arising from its strong \mathcal{Z}_2 symmetry. Finite values of Δ or κ_ϕ act only within the blocks \mathcal{L}_0^{+-} and \mathcal{L}_0^{-+} , so that the four-block-diagonal structure of \mathcal{L}_0 is preserved. The single-photon loss κ_1 , instead, connects different blocks, resulting in a two-block-diagonal structure typical of weakly \mathcal{Z}_2 -symmetric systems.

environment [9, 16, 54]. These processes are modeled by the Lindblad master equation [4, 55–57]:

$$\partial_t \hat{\rho} = \mathcal{L} \hat{\rho} = \mathcal{L}_0 \hat{\rho} + \mathcal{L}_1(\kappa_1, \kappa_\phi) \hat{\rho} \quad (2a)$$

$$\mathcal{L}_0 \hat{\rho} = -i[\hat{H}, \hat{\rho}] + \eta \mathcal{D}[\hat{a}^2] \hat{\rho} \quad (2b)$$

$$\hat{H} = \Delta \hat{a}^\dagger \hat{a} + \frac{G^*}{2} \hat{a}^2 + \frac{G}{2} (\hat{a}^\dagger)^2 - \frac{U}{2} (\hat{a}^\dagger)^2 \hat{a}^2 \quad (2c)$$

$$\mathcal{L}_1(\kappa_1, \kappa_\phi) \hat{\rho} = \kappa_1 \mathcal{D}[\hat{a}] \hat{\rho} + \kappa_\phi \mathcal{D}[\hat{a}^\dagger \hat{a}] \hat{\rho}, \quad (2d)$$

Here, $\hat{\rho} \equiv \hat{\rho}(t)$ (for brevity) is the system density matrix at time t and \mathcal{L} is the Liouvillian superoperator. \mathcal{L}_0 is the confining part, where an Hamiltonian \hat{H} describes the coherent dynamics, characterized by the two-photon driving field amplitude G , the Kerr nonlinearity U , and the pump-to-cavity detuning Δ . \mathcal{L}_0 also accounts for two-photon losses, with η being the rate at which pairs of photons are incoherently emitted. The dissipator $\mathcal{D}[\hat{\Gamma}]$, with jump operator $\hat{\Gamma}$, acts as

$$\mathcal{D}[\hat{\Gamma}] \hat{\rho} = \hat{\Gamma} \hat{\rho} \hat{\Gamma}^\dagger - \frac{\hat{\Gamma}^\dagger \hat{\Gamma} \hat{\rho} + \hat{\rho} \hat{\Gamma}^\dagger \hat{\Gamma}}{2}. \quad (3)$$

$\mathcal{L}_1(\kappa_1, \kappa_\phi)$ describes, instead, unwanted effect of the environment on the code, inducing errors in the logical qubit. While κ_1 is the single photon loss rate, κ_ϕ describes the total dephasing rate of the encoding mode. The combined effect of \mathcal{L}_0 and \mathcal{L}_1 is usually recast in terms of a bit-flip error rate γ_1 , and a phase-flip error rate γ_ϕ , acting on the logical qubit [9].

A. Liouvillian spectrum and symmetries

Liouvillian symmetries are distinguished into two classes: *weak* and *strong* symmetries [31, 58–63]. A weak symmetry occurs when an operator \hat{O} obeys $\mathcal{L}(\hat{O} \hat{\rho} \hat{O}^\dagger) =$

$\hat{O}(\mathcal{L} \hat{\rho}) \hat{O}^\dagger$, where $\mathcal{L} \hat{\rho} = -i[\hat{H}, \hat{\rho}] + \sum_j \gamma_j \mathcal{D}[\hat{\Gamma}_j] \hat{\rho}$. A strong symmetry, on the other hand, requires $[\hat{O}, \hat{H}] = [\hat{O}, \hat{\Gamma}_j] = 0$. While a weak symmetry only guarantees the existence of a single steady state, a strong symmetry induces a n -dimensional steady-state manifold, with n the number of non-equivalent irreducible representations of the symmetry group [63].

The ideal Liouvillian \mathcal{L}_0 described in Eq. (2)(b) is characterized by a *strong* \mathcal{Z}_2 symmetry, as both the Hamiltonian and the jump operators are invariant under the transformation $\hat{a} \rightarrow -\hat{a}$, and thus they both commute with the parity operator $\hat{\Pi}$ [62, 64]. The Hilbert space can then be decomposed as $\mathcal{H} = \bigoplus_{\mu \in \{\pm\}} \mathcal{H}_\mu$, where \mathcal{H}_\pm are the subspaces spanned by even and odd parity eigenstates respectively. Correspondingly, the space of linear operators acting on \mathcal{H} can be decomposed into four subspaces $\mathcal{B}_{\mu\nu}$. The strong symmetry ensures that $\mathcal{B}_{\mu\nu}$ are invariant under the action of the Liouvillian, i.e., $\mathcal{L}_0(\mathcal{B}_{\mu\nu}) \subset \mathcal{B}_{\mu\nu}$. Thus, the Liouvillian can be decomposed in the block-diagonal form $\mathcal{L}_0 = \mathcal{L}_0^{++} \oplus \mathcal{L}_0^{+-} \oplus \mathcal{L}_0^{-+} \oplus \mathcal{L}_0^{--}$ sketched in Fig. 1(b).

The dynamics within each Liouvillian block is conveniently described in terms of its eigenvalues $\lambda_n^{\mu\nu}$ and right eigenoperators $\hat{\rho}_n^{\mu\nu}$ where

$$\mathcal{L}_0^{\mu\nu} \hat{\rho}_n^{\mu\nu} = \lambda_n^{\mu\nu} \hat{\rho}_n^{\mu\nu} \quad \text{with} \quad -\text{Re}\{\lambda_n^{\mu\nu}\} < -\text{Re}\{\lambda_{n+1}^{\mu\nu}\}. \quad (4)$$

While the imaginary part of $\lambda_n^{\mu\nu}$ describes the oscillations within the specified sector, its negative real part gives the relaxation rate towards the steady state. Throughout the paper, we deem

$$\Lambda_n^{\mu\nu} = -\text{Re}\{\lambda_n^{\mu\nu}\}. \quad (5)$$

Due to the strong symmetry, $\hat{\rho}_n^{\mu\nu}$ are also eigenoperators of $\hat{\Pi}$ according to the relation

$$\hat{\Pi} \hat{\rho}_n^{\mu\nu} = \mu \hat{\rho}_n^{\mu\nu}, \quad \text{and} \quad \hat{\rho}_n^{\mu\nu} \hat{\Pi}^\dagger = \nu \hat{\rho}_n^{\mu\nu}. \quad (6)$$

From here on, we shall refer to $\hat{\rho}_0^{\mu\mu}$ as *steady states* and to $\hat{\rho}_0^{\mu\nu}$, with $\mu \neq \nu$, as *coherences* [23, 64].

B. Encoding quantum information in a bosonic state

On general grounds, an open quantum system can indefinitely encode quantum information if its dynamics is isomorphic to that of a *noiseless subsystem* (NS) [1, 13, 22, 65–68]. The general density matrix structure encapsulating the above properties is of the type

$$\hat{\rho} = \hat{Q} \otimes \hat{M} = \begin{pmatrix} Q_{++} & Q_{+-} \\ Q_{-+} & Q_{--} \end{pmatrix} \otimes \hat{M}, \quad (7)$$

with $Q_{++} + Q_{--} = 1$. The matrix $\hat{\rho}$ is that of a bipartite system, where \hat{Q} is the logical qubit encoding quantum information, and is stationary if no gate operation is applied. \hat{M} , on the other hand, is typically a mixed state

and can evolve in time. In an open system, the presence of a NS is directly linked to the existence of a steady state degeneracy in the Liouvillian, resulting in infinitely long lived steady states and coherences.

For a \mathcal{Z}_2 -symmetric Liouvillian, this condition requires a zero eigenvalue in each symmetry sector, i.e., $\mathcal{L}_0 \hat{\rho}_0^{\mu\nu} = 0$ $\forall \mu, \nu \in \{\pm\}$. Q is then expressed as

$$Q_{\mu\nu} = \text{Tr}\left\{(\hat{J}_0^{\mu\nu})^\dagger \hat{\rho}(0)\right\} = \text{Tr}\left\{(\hat{J}_0^{\mu\nu})^\dagger \hat{\rho}(t)\right\}, \quad (8)$$

where $\hat{J}_n^{\mu\nu}$ are the left eigenoperators of \mathcal{L}_0 , defined by

$$\hat{J}_n^{\mu\nu} \mathcal{L}_0^{\mu\nu} = (\mathcal{L}_0^{\mu\nu})^\dagger \hat{J}_n^{\mu\nu} = (\lambda_n^{\mu\nu})^* \hat{J}_n^{\mu\nu}. \quad (9)$$

These form a basis onto which the time-evolution of observables in the Heisenberg picture can be expanded, and are related to $\hat{\rho}_n^{\mu\nu}$ by the bi-orthogonality relation

$$\text{Tr}\left\{(\hat{J}_n^{\mu\nu})^\dagger \hat{\rho}_m^{\mu'\nu'}\right\} = \delta_{\mu,\mu'} \delta_{\nu,\nu'} \delta_{m,n}. \quad (10)$$

The null-eigenoperators $\{\hat{J}_0^{\mu\nu}\}_{\mu,\nu}$ of \mathcal{L}^\dagger , in particular, are conserved quantities, i.e. the observables which remain constant throughout the evolution. A strong symmetry ensures the existence of at least n conserved quantities [64].

C. Choice of parameters for dissipative, Hamiltonian, and hybrid confinement

In the search for the optimal working parameters of a given bosonic code, the following set of criteria should be fulfilled:

- (C1) The steady-state manifold of the Liouvillian \mathcal{L}_0 should approximately realize the NS structure in Eq. (7).
- (C2) The detrimental effect of the environment on the encoded quantum information, described by the Liouvillian \mathcal{L}_1 , should be minimal. As a quantifier of this effect we propose the channel-fidelity decay rate (Sec. IID).
- (C3) The fidelity of quantum gates on the logical qubit, which is a trade-off between the speed at which logical operations are carried out and the leakage out of the code manifold during their action, should be maximized.
- (C4) The regime of operation of the single qubit should be compatible with the operation of coupled qubits, necessary for two-qubit gates and concatenated error correction codes [19, 27, 69–72].

Based on these considerations, two main approaches to generate and stabilize the cat manifold have been proposed. In *Dissipative stabilization* ($\eta \neq 0$) [9, 17, 18], operating at $\Delta = 0$ makes Eq. (7) exactly fulfilled [9],

so that any initial state $\hat{\rho}(0)$ evolves toward the manifold spanned by the exact steady states and coherences $\hat{\rho}_0^{\mu\nu} = |\mathcal{C}_\alpha^\mu\rangle\langle\mathcal{C}_\alpha^\nu|$, with [32, 45]

$$\alpha(\Delta = 0) = \sqrt{-\frac{G}{U - i\eta}}. \quad (11)$$

For dissipative stabilization, the strength U of the non-linearity is minimized, so to maximize the size of the cat. Note that U can never be completely eliminated without also switching-off G (see microscopic constraints in App. A). The main advantage of this protocol is its intrinsic resistance to leakage processes, and an exponential suppression of the logical phase-flip error rate in the cat size, namely

$$\gamma_\phi = \kappa_1 |\alpha|^2 e^{-4|\alpha|^2} + \kappa_\phi |\alpha|^2 e^{-2|\alpha|^2}. \quad (12)$$

Its main drawback, however, is the limited performance of logical gates on current superconducting platforms [18, 24, 70].

A different approach to the generation and stabilization of the cat manifold, that partially sidelines the necessity for a quadratic dissipation channel, is the *Kerr-cat qubit* [25, 27]. In Kerr-cat qubits, the logical information is encoded within the two-fold degenerate ground state of a purely Hamiltonian, quadratically driven Kerr-nonlinear oscillator ($\Delta = 0, \eta = 0$). The energy gap separating the ground manifold (spanned by cat states of opposite parity) from the excited states is proportional to G and U [26]. This energy separation is pivotal for a reliable encoding of the information, in the realization of fast gates, and quantum non-demolition readout [28]. Leakage to higher excited states outside of the cat manifold, however, inevitably degrades quantum information and limits the performance of the Kerr-cat code [28]. In particular, it can be shown that the effect of dephasing is no longer exponentially suppressed, as an effect of the Kerr nonlinearity, so that

$$\gamma_\phi = \kappa_1 |\alpha|^2 e^{-4|\alpha|^2} + \kappa_\phi |\alpha|^2. \quad (13)$$

Generalizing the idea of a Kerr stabilization, a *hybrid* confinement mechanism, combining both Kerr and dissipative confinement, has recently been proposed [24]. It was shown, however, that the values of U for which the exponential suppression of γ_ϕ in $|\alpha|^2$ still holds, are far too small to provide an advantage over a purely dissipative scheme.

D. Channel-fidelity rate

The NS condition Eq. (7) is rarely exactly met, especially in the presence of errors. This calls for the definition of an estimator capable of quantitatively assessing the resistance of the code to both Hamiltonian and dissipative processes.

An established estimator of the code's performance is the channel-fidelity [15]. Over a time interval t , the channel-fidelity is defined as

$$\mathcal{F} = \frac{1}{4} \text{Tr}\{\mathcal{E}\} = \frac{1}{4} \text{Tr}\{\mathcal{S}_{\text{code}}^{-1} \circ e^{\mathcal{L}t} \circ \mathcal{S}_{\text{code}}\}. \quad (14)$$

Here, \mathcal{E} is the quantum channel governing all noise, recovery and Liouvillian evolution processes acting on the logical qubit. $\mathcal{S}_{\text{code}}$ is the superoperator representing the encoding from the bosonic space onto the logical qubit defined by the ideal Liouvillian \mathcal{L}_0 . Note that $\mathcal{S}_{\text{code}}$ and its "inverse" are not standard superoperators, as they map the logical two-dimensional basis $\{|0_L\rangle, |1_L\rangle\}$ to the infinite-dimensional bosonic space spanned by, e.g., the Fock states $\{|0\rangle, |1\rangle, |2\rangle, \dots\}$. In the case of Schrödinger cat qubits, we have

$$\mathcal{S}_{\text{code}} = \sum_{\mu, \nu = \pm} \|\rho_0^{\mu\nu}\rangle\rangle \langle\langle \mu\nu \|, \quad \mathcal{S}_{\text{code}}^{-1} = \sum_{\mu, \nu = \pm} \|\mu\nu\rangle\rangle \langle\langle J_0^{\mu\nu} \|, \quad (15)$$

where $\|\mu\nu\rangle\rangle = \text{vec}(|\mu\rangle\langle\nu|)$ are the matrix elements of \hat{Q} in Eq. (7), and $\|A\rangle\rangle = \text{vec}(\hat{A})$ is the vectorization of an operator \hat{A} [23, 73]. It follows that

$$\mathcal{S}_{\text{code}} \mathcal{S}_{\text{code}}^{-1} = \sum_{\mu\nu} \|\rho_0^{\mu\nu}\rangle\rangle \langle\langle J_0^{\mu\nu} \| = \mathcal{P}_L, \quad (16)$$

where \mathcal{P}_L is the superoperator projecting onto the logical manifold [as it follows from Eq. (10)].

Within this picture, we can thus introduce the channel infidelity rate as

$$\mathcal{R} = \frac{\partial}{\partial t} (1 - \mathcal{F})|_{t=0} = -\frac{1}{4} \text{Tr}\{\mathcal{P}_L \mathcal{L}\}, \quad (17)$$

where we used the cyclic property of the trace.

The infidelity rate can be written as the sum of the phase- and bit-flip contributions as $\mathcal{R} = \mathcal{R}_\phi + \mathcal{R}_1$ with

$$\begin{aligned} \mathcal{R}_\phi &= -\frac{1}{4} \sum_{\mu} \langle\langle J_0^{\mu\bar{\mu}} \| \mathcal{L} \| \rho_0^{\mu\bar{\mu}} \rangle\rangle, \\ \mathcal{R}_1 &= -\frac{1}{4} \sum_{\mu} \langle\langle J_0^{\mu\mu} \| \mathcal{L} \| \rho_0^{\mu\mu} \rangle\rangle, \end{aligned} \quad (18)$$

and $\overline{(\mu = \pm)} = \mp$.

The logical bit- and phase-flip error rates γ_1 and γ_ϕ have been often extrapolated from the long-time dynamics of the conserved quantities $\hat{J}_x = \hat{J}_0^{+-} + \hat{J}_0^{-+}$ and $\hat{J}_z = \hat{J}_0^{++} - \hat{J}_0^{--}$ [24]. We remark that this approach is however oblivious to the effect of transient losses in the short-time dynamics, that can dominate in determining the performance of the code. As we will show in Sec. V, the quantity (17) is a more accurate estimator of the performance of the code in cases where the decay of the fidelity is characterized by multiple timescales, while in regimes where only one timescale is relevant both estimators give the same results.

III. THE CRITICAL CAT CODE

Dissipative, Hamiltonian, and hybrid stabilization alike, operate at $\Delta = 0$, where (C1) is exactly met. None of them, however, simultaneously fulfill (C2-C4). Here, we identify a hybrid regime – the *critical cat qubit* – where (C1) is only approximately fulfilled, but (C2-C4) are significantly improved. Its features are a sizeable Kerr nonlinearity U , comparable to the two-photon loss rate η , and finite values of the detuning Δ . In this section, we demonstrate that the efficient encoding of quantum information is not limited to $\Delta = 0$, but rather extends over a broad range of values of the detuning, thus fulfilling condition (C1). Although operated in a hybrid regime where both nonlinearity and dissipation are sizable, thanks to the finite value of Δ the critical cat qubit is not subject to the limitations outlined in Ref. [24]. In particular, the encoding is characterized by an enhanced exponential suppression of dephasing errors, thus fulfilling (C2), while the sizeable Kerr nonlinearity enables faster gate operations, as required by (C3). Finally we will show how, by operating in the vicinity of a dissipative phase transition, the critical cat qubit is also resilient to random frequency shifts that may be introduced by Kerr-coupled qubits, thus fulfilling condition (C4).

A. Liouvillian analysis of the ideal critical dissipative cat

In order to provide a thorough analysis of the competing effect of U , η , and/or Δ , we analyze the spectral properties of \mathcal{L}_0 , momentarily forgoing the microscopic constraints of actual experimental platforms discussed in App. A. A detailed analysis of the code for physically viable parameters is presented in App. B. For a fixed G , we set

$$\eta = W \cos(\theta), \quad U = W \sin(\theta), \quad \eta^2 + U^2 = W^2. \quad (19)$$

W then represents an effective nonlinearity at $\Delta = 0$. A constant W results in all configurations having the same photon number at $\Delta = 0$ [c.f. Eq. (11)]. Then, the parameter θ allows to continuously explore the intermediate region between the weakly- and strongly-nonlinear limits. The results of the analysis are summarized in Fig. 2 where the yellow curves represent the case of a purely dissipative cat ($U = 0$), while darker curves correspond to larger values of the Kerr nonlinearity.

Figure 2(a) displays the average photon number as a function of Δ . For $U = 0$, the system passes from an almost-empty cavity for $|\Delta| > G$ to a finite photon number. The maximal photon number is attained at $\Delta = 0$. Contrarily to the $\Delta = 0$ case, where increasing G is the only way to increase the size of the cat, for $U \neq 0$ larger cats occur for $\Delta > 0$. The photon number increases up to $\Delta/G \simeq \sqrt{1 + (U/\eta)^2}$, then abruptly jumps to zero.

The loss of quantum information is determined by the slowest (possibly vanishing) relaxation rate of each sym-

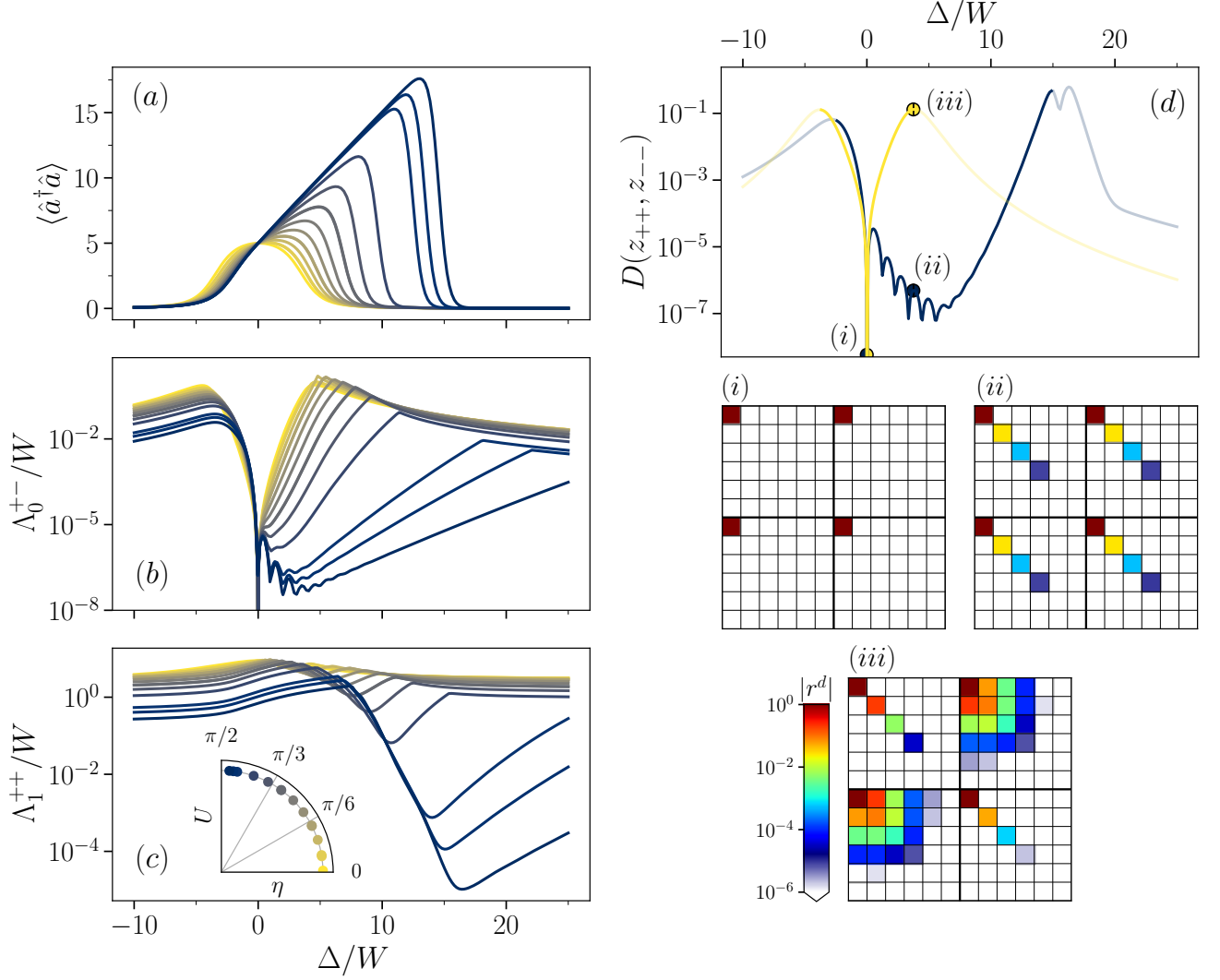


FIG. 2. Spectral analysis of the Liouvillian. For all plots, $G/W = 5$. (a) Average occupation of the cavity as a function of the detuning Δ for different values of the Kerr nonlinearity U and the two-photon dissipation η satisfying Eq. (19). As $|\alpha(\Delta=0)|^2 = G/W$, all curves intersect at $\Delta = 0$ [c.f. Eq. (11)]. The jump in $\langle \hat{a}^\dagger \hat{a} \rangle$ appearing at $\Delta > 0$ becomes sharper for larger values of θ , heralding the occurrence of a first-order phase transition. (b) Liouvillian gap of the $+-$ symmetry sector. The width of the broken-symmetry region gradually increases with U . Optimal configurations with non-vanishing detuning appear as local minima of the curves and allow taking advantage of the strong nonlinearity (see text). (c) Liouvillian gap of the $++$ symmetry sector. Its closure, for increasing values of U , highlights the first-order nature of the phase transition. (d) Trace norm $D(z_{++}, z_{--})$, defined in the main text, as a function of Δ and for $2\theta/\pi = 0.01, 0.96$. The insets show the structure of the full density matrix for the points indicated in the main figure. (i) exemplifies a DFS, (ii) a NS, and (iii) a configuration where quantum information cannot be encoded.

metry sector, i.e. by $\Lambda_0^{\mu\nu}$ [c.f. Eq. (5)]. While the strong \mathbb{Z}_2 symmetry ensures $\Lambda_0^{++} = \Lambda_0^{--} = 0$, the off-diagonal Liouvillian gap $\Lambda_0^{\pm,\mp}$ can still take finite values and should be minimized in order to suppress the qubit decoherence. In Fig. 2(c) we display $\Lambda_0^{+-} = \Lambda_0^{-+}$ as a function of Δ for different choices of the ratio U/η . Notice that although $\Lambda_0^{+-} = 0$ at $\Delta = 0$ for all values of U , it rapidly increases if $\Delta \neq 0$. For increasing U , however, Λ_0^{+-} becomes progressively smaller over an increasingly

larger region of positive values of Δ where quantum information may be encoded.

Lastly, we provide numerical evidence of the existence of a NS tensor structure [c.f. Eq. (7)]. In the ideal NS case, the eigenoperators $\hat{\rho}_0^{\mu\nu}$ need to obey [31]

$$\hat{U}_\mu \rho_0^{\mu\nu} \hat{U}_\nu^\dagger \equiv |\mu\rangle\langle\nu| \otimes z_{\mu\nu}, \quad (20)$$

where $z_{\mu\nu} = z_{\mu'\nu'} \forall \mu, \nu, \mu', \nu'$ and \hat{U}_μ is the unitary transformation diagonalizing the density matrix $\hat{\rho}_0^{\mu\mu}$ [74].

We quantify the discrepancy from this ideal case using the trace distance $D(A, B) = \sqrt{\text{Tr}\{(A - B)^\dagger(A - B)\}}$ between the two diagonal blocks z_{++} and z_{--} . $D(z_{++}, z_{--})$ is plotted in Fig. 2(d) for the cases $2\theta/\pi = 0.96, 0.01$. The former case displays small values of $D(z_{++}, z_{--})$ over the whole region where Λ_{\pm} is small, while for $U \simeq 0$, $D(z_{++}, z_{--})$ only vanishes close to $\Delta = 0$. Similar results were found for $D(z_{++}, z_{+-})$ (not shown). The insets below Fig. 2(d) are color plots of the absolute value of the matrix elements, for the three cases highlighted in the plot.

We conclude that a cat-like state can be generated, capable of encoding quantum information, in a whole region of $-G < \Delta < G\sqrt{1 + (U/\eta)^2}$. Although this state is not exactly the ideal cat described in Eq. (1), it nonetheless displays analogous properties.

Finally, we remark that having performed this analysis in the absence of errors ($\kappa_\phi = \kappa_1 = 0$), the off-diagonal gap is a measure of information loss equivalent to the infidelity rate, i.e., $\mathcal{R} = \mathcal{R}_\phi = \Lambda_{+-}/2$.

Appendix C shows that the same gates that act on the dissipative and Kerr cat qubit can be straightforwardly applied to the critical cat.

B. Connection with first-order dissipative phase transitions

As detailed in Sec. II B, a necessary condition to encode quantum information is the presence of a vanishing eigenvalue in each of the four Liouvillian symmetry sectors. Zero eigenvalues are not only the hallmark of quantum information encoding, but also one of the main signatures of a dissipative phase transition – a non-analytical change in the properties of an open quantum system as a function of one of its parameters [32, 41]. Two types of critical phenomena can occur in open quantum systems: first- and second-order phase transitions. The former (latter) corresponds to a discontinuous (continuous, but not differentiable) change in the system's properties. Despite their innate differences, both first- and second-order transitions can present with [32] or without [42] spontaneous symmetry breaking (SSB).

The normal phase of a *weakly symmetric* system is generally characterized by a unique steady state. For a weak \mathcal{Z}_n symmetry, SSB causes the emergence of $n - 1$ additional zero eigenvalues of the Liouvillian, bringing the dimension of the system's steady state manifold to n , thus realizing a so called $1 \rightarrow n$ transition [31]. However, no quantum information can be stored into this manifold, as the coherences rapidly decay. Quantum information can instead be stored within the *broken symmetry phase* of a system characterized by a *strong symmetry*, which supports classical information encoding in its normal phase. In this case, for a \mathcal{Z}_n symmetry, there always exist n steady states of the system, which become n^2 upon SSB, thereby realizing a so called $n \rightarrow n^2$ transition [31]. In the present case of the \mathcal{Z}_2 strongly symmetric Kerr res-

onator, the $n \rightarrow n^2$ transition gives rise to the NS qubit structure in Eq. (7). Even though criticality is only defined in the thermodynamic limit, precursors of DPTs arise in *finite-size* systems.

In the $U = 0$ case, also investigated in Ref. [31], the system displays *two* second-order phase transitions between vacuum- and cat-like states in the limit of $G/\eta \gg 1$. These transitions emerge from a competition between G and Δ [34, 75–77] and do not depend on $\text{sgn}(\Delta)$. Indeed, as detailed by the yellow curves in Fig. 2, two critical points located at $\Delta/G = \pm 1$ symmetrically divide the phase space into a normal region ($|\Delta|/G > 1$), hosting at most a classical qubit structure, and a \mathcal{Z}_2 -broken region ($|\Delta|/G < 1$), where Λ_0^{+-} is small (zero in the TDL) and an approximate (exact in the TDL) NS structure emerges. For such vanishing nonlinearities the broken symmetry region is very narrow, the maximal photon number is attained at $\Delta = 0$, and can be only increased by increasing the ratio G/η . In actual experimental realizations, however, G is technologically limited by the fact that a large driving field would unavoidably activate higher order non-linear spurious processes in Eq. (2), thereby degrading the cat code structure.

For finite U , the behaviour of the system significantly changes. While the phase boundary at negative values of Δ is not significantly modified, and the corresponding DPT is still of second order, for positive Δ a *first-order* transition at $\Delta/G \simeq \sqrt{1 + (U/\eta)^2}$ replaces the second order one found at $\Delta/G = 1$ for $U = 0$. Indeed, the extent of the \mathcal{Z}_2 -broken region wherein Λ_{+-} vanishes in the TDL, is seen to increase with U far beyond the typical values obtained for $U \simeq 0$ [Fig. 2(b)]. Further signs of the gradual transition from a second to a first-order DPT are the elbow-like shape of the photon number for $U = 0$ in Fig. 2(a), gradually evolving into a jump discontinuity for increasing values of U , and the precursors to a point-like closure [32] of the diagonal gap Λ_1^{++} seen in Fig. 2(c).

In this regard, the use of a first-order DPT entails several advantages with respect to the proposal of Ref. [31]. First, the \mathcal{Z}_2 -broken symmetry region becomes progressively larger for an increasing nonlinearity. Second, a sizeable increase of the steady-state photon number occurs in the symmetry-broken phase, and over a wide range of positive values of the detuning close to the boundary of the first-order DPT. Furthermore, large values of Δ can be obtained with far less stringent condition than those limiting G (see Appendix A), providing an on-demand resource to reach large critical cats.

C. Resistance to frequency shifts

As discussed in Ref. [31], random shifts in the resonant frequency of the oscillator can significantly hinder the code's performance. In most cases, these effects can be modeled by an additional correlated noise in the form of an effective detuning $\Delta_{\text{err}} \hat{a}^\dagger \hat{a}$. Common sources of shifts are cross-Kerr interactions originating either from spu-

rious interactions with dissipatively coupled qubits, or from stochastic jumps and thermal excitations in reservoir modes nonlinearly coupled to the system by, e.g., Josephson junctions. Because quantum information can be efficiently encoded over the whole broken symmetry region, we anticipate the effect of such shifts to be far less detrimental for the critical cat code, where the broken symmetry region is far broader than in the purely dissipative case. To demonstrate this, we consider the following protocol. The system is initialized in the state $\hat{\rho}(0) = |+_L\rangle\langle+_L|$, with $|\pm_L\rangle = (|0_L\rangle \pm |1_L\rangle)/\sqrt{2}$. The logical encoding is taken with respect to the manifold stabilized by the bare Liouvillian \mathcal{L}_0 , and the corresponding $\hat{Q}(0)$ matrix is computed using Eq. (7). The system is quenched with an additional detuning Δ_{err} and evolves under $\mathcal{L}'\hat{\rho} = \mathcal{L}_0\hat{\rho} - i\Delta_{\text{err}}[\hat{a}^\dagger\hat{a}, \hat{\rho}]$ for a time $t_0 = 10/W$. Finally, Δ_{err} is switched off, and the system is let thermalize under \mathcal{L}_0 for a time $t_1 = 5/W$.

Figure 3 shows the orthogonality $1 - O$ as a function of Δ for different choices of U and η parametrized by Eq. (19). O is the overlap between the initial and the final states, and is defined by [78]

$$O = \text{Tr}\{\hat{\rho}(0), \hat{\rho}(t_0 + t_1)\} = \text{Tr}\left\{\hat{\rho}(0)e^{\mathcal{L}_0 t_1}e^{\mathcal{L}' t_0}\hat{\rho}(0)\right\}. \quad (21)$$

Fig. 3(a) shows the quantity $1 - O$ as computed for $\Delta_{\text{err}} = W$. The black contour line encircles the region $1 - O < 10^{-5}$. Given the random nature of shifts, we also consider $\Delta_{\text{err}} = -W$, for which the isoline $1 - O < 10^{-5}$ is overlaid in white. The data clearly identify a range of parameters in which quantum information encoded in the critical cat is highly resilient to random frequency shifts. This region is characterized by positive values of Δ and $U/\eta \sim 1$. The plot in Fig. 3(b) shows the same quantities for $|\Delta_{\text{err}}| = 4W$. Again, we observe that a finite value of U is necessary for an optimal performance of the code in the presence of random frequency shifts.

IV. ENHANCED SUPPRESSION OF DEPHASING ERRORS

We now study how the critical cat fares in the presence of a dephasing rate κ_ϕ , while assuming $\kappa_1 = 0$ [cf. Eq. (2)]. Dephasing is a process that conserves parity, and thus the strong symmetry of the Liouvillian. It results, therefore, in two steady states $\hat{\rho}_0^{\mu\mu}$, but not in a stabilized qubit manifold, even for $\Delta = 0$. Indeed, the Liouvillian admits only two conserved quantities $\hat{J}_0^{\mu\mu}$, while $\hat{J}_0^{\mu\nu}$ ($\nu \neq \mu$) decay, as do $\hat{\rho}_0^{\mu\nu}$. This directly translates into an effective phase-flip rate γ_ϕ on the logical qubit, whose value is determined by the combined effect of dephasing and of detuning.

A key feature of cat states at $\Delta = 0$ is the exponential suppression of γ_ϕ in the size of the cat. For $U = 0$, and small values of κ_ϕ , first-order perturbation theory leads to Eq. (12) [9]. This feature is displayed in Fig. 4(a),

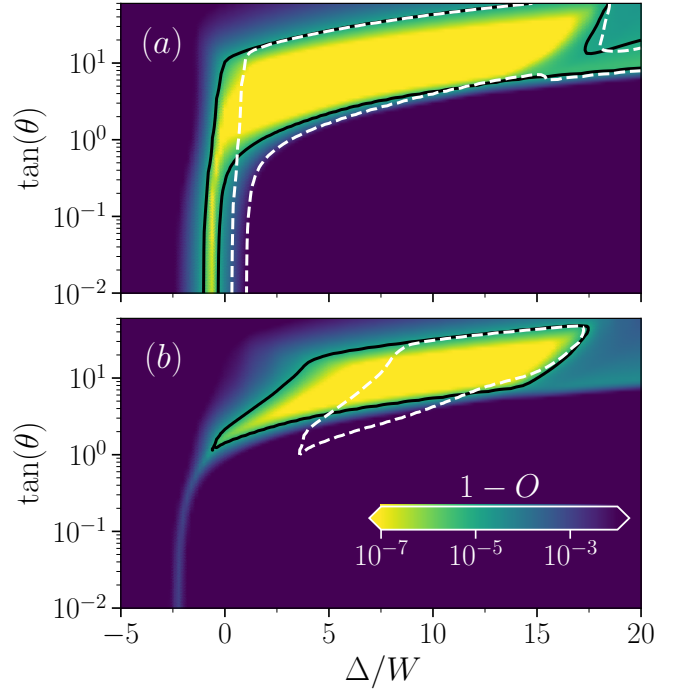


FIG. 3. The quantity $1 - O$, defined in Eq. (21), displayed as a function of the detuning Δ and of the angle θ in Eq. (19). The initial state $|+_L\rangle$, and the final state obtained from the recovery procedure, are detailed in the main text. The data in the two panels were computed assuming a frequency shift of (a) $\Delta_{\text{err}} = W$ and (b) $\Delta_{\text{err}} = 4W$. In both panels, the black isolines bound the region $1 - O < 10^{-5}$ for $\Delta_{\text{err}} > 0$. The white dashed lines bound the same region in the cases (a) $\Delta_{\text{err}} = -W$ and (b) $\Delta_{\text{err}} = -4W$.

where the dashed lines represent γ_ϕ as a function of G for $\Delta = U = 0$, and several values of κ_ϕ [79].

Equation (12), however, only holds for $\Delta = U = 0$ and $\kappa_\phi \ll W$. To study the critical cat, we numerically diagonalize the Liouvillian and, for each value of G , we select the optimal detuning Δ_{opt} that minimizes γ_ϕ . We find that Δ_{opt} approximately obeys

$$\Delta_{\text{opt}}(G, \kappa_\phi, \theta) \approx \beta(\kappa_\phi, \theta) \times G \cdot \Theta(G - G_c(\kappa_\phi, \theta)), \quad (22)$$

where $\beta(\kappa_\phi, \theta)$ does not depend on G , Θ is the Heaviside step function, and $G_c(\kappa_\phi, \theta)$ is the critical value of the first-order DPT (see also Fig. 6). This feature is highlighted by Fig. 4(b), where the ratio $\gamma_\phi(\Delta)/\gamma_\phi(0)$ is plotted as a function of Δ/G for different values of G and $\kappa_\phi/W = 10^{-3}$. The optimal value of Δ jumps from $\Delta_{\text{opt}} = 0$ to $\Delta_{\text{opt}} \simeq G/2$ upon crossing $G_c \simeq 1.96W$. The solid lines in Fig. 4(a) show $\gamma_\phi = \Lambda_0^{+-}$ for the critical cat, obtained by exact diagonalization of \mathcal{L}_0^{+-} , for $2\theta/\pi = 0.88$. After an initial plateau, γ_ϕ exponentially decays as a function of the photon number. All curves nearly overlap, showing that γ_ϕ is almost unaffected by κ_ϕ in the range of values considered. This is not the case for $\Delta = U = 0$, where γ_ϕ increases *linearly* with κ_ϕ , as inferred both from Eq. (12) and from the data in

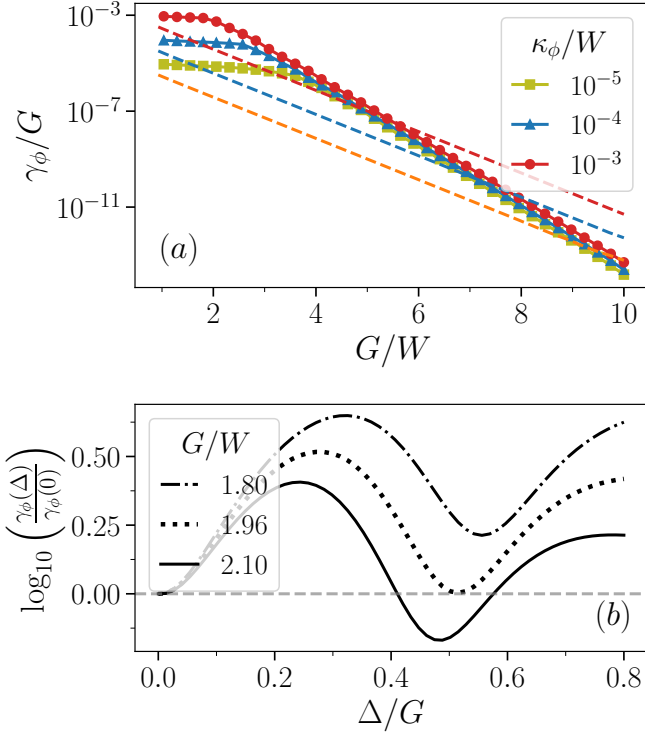


FIG. 4. Exponential suppression of the phase-flip error rate γ_ϕ as a function of the two-photon driving amplitude G for a selection of values of the dephasing rates κ_ϕ , detuning values Δ , and confinement scheme θ [see Eq. (19)]. (a) γ_ϕ as a function of the resonant photon number $n(\Delta = 0) = G/W$ for the case of dissipative confinement $\Delta = 0$, $2\theta/\pi = 0.01$ (dashed lines), and hybrid-critical confinement $\Delta = \Delta_{\text{opt}}$, $2\theta/\pi = 0.88$ (full markers). A global optimization algorithm is used to select the optimal detuning value Δ_{opt} for each value of G . (b) Phase-flip error rate γ_ϕ as a function of Δ/G for $G/W = 1.8, 1.958$, and 2.1 . For visual clarity, all curves in the inset have been normalized to their value at resonance.

Fig. 4(a). Assuming γ_ϕ to follow the law:

$$\gamma_\phi(\Delta_{\text{opt}}, G) = \gamma_0 G \exp\{-\zeta(\kappa_\phi, \theta)G\}. \quad (23)$$

we use this relation to extract the scaling coefficient ζ .

In Fig. 5, ζ is plotted as a function of $\tan(\theta) = U/\eta$ for $\kappa_\phi/W = 10^{-2}$ for both the optimal and resonant detuning configurations. As predicted in Ref. [24], for $\Delta = 0$ the system loses its protection against dephasing-induced phase-flip errors as it gradually transitions from a dissipative to a Hamiltonian confinement regime (orange curve). On the contrary, the critical cat operated at $\Delta = \Delta_{\text{opt}}(G)$ and $U \sim \eta$ endows the system with an additional resilience to errors, so that the phase-flip error rate is exponentially suppressed with an enhanced scaling coefficient with respect to its base value of $\zeta = 2$ in the purely dissipative regime (blue curve at $\theta = 0$). The exponential suppression of γ_ϕ in Eq. (23) still holds, though with a reduced exponential rate ζ , if the detuning is not set to its optimal value. Fig. 6 shows the phase-flip rate γ_ϕ and the average photon occupation, as computed

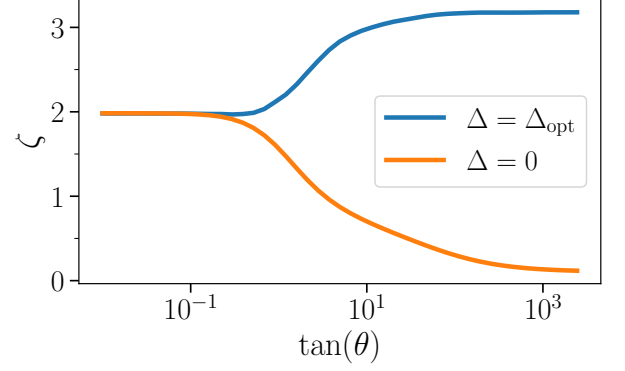


FIG. 5. The coefficient ζ , expressing the rate of exponential suppression of γ_ϕ in the cavity's population, as defined in Eq. (23), is computed as a function of $\tan(\theta) = U/\eta$ for $\kappa_\phi = 10^{-2}W$. The orange curve details the behaviour of ζ when varying θ continuously from a dissipative to a Hamiltonian confinement, as computed for $\Delta = 0$. The same quantity, evaluated for the optimal detuning Δ_{opt} , is shown in blue.

for $\Delta/W = 4$. The sudden increase of the photon occupation in Fig. 6(b) reveals the critical point G_c where the first-order DPT takes place. The rate γ_ϕ in Fig. 6(a) peaks at $G \simeq G_c$. For $G \gtrsim G_c$, Eq. (22) predicts an optimal detuning value $\Delta_{\text{min}}/W \simeq 4$, resulting in a steep exponential decay of γ_ϕ with G . The decay is slower for still larger values of G , as in this regime the optimal detuning value predicted by Eq. (22) is significantly larger than $\Delta/W = 4$.

These results provide clear evidence of the exponential suppression of γ_ϕ as a function of the cat size in the critical dissipative regime. The increased coefficient ζ , as well as the independence of γ_ϕ on κ_ϕ , demonstrate the enhanced performance of the code in the critical regime. We notice in passing that, in the absence of single particle loss, γ_ϕ and $\mathcal{R} = \mathcal{R}_\phi$ are equivalent measures of the retention of quantum information under errors, as $\gamma_\phi = 2\mathcal{R}_\phi = \Lambda_0^{+-} = \Lambda_0^{-+}$.

Assuming now a constant value of G – which is an experimental resource – we can quantify the advantage brought by the critical cat for varying values of U/η and κ_ϕ . In Fig. 7 we display the channel-fidelity leakage $\mathcal{R}_\phi(\Delta_{\text{opt}})$ when operating at optimal detuning, as a function of U/η and κ_ϕ . The quantity is normalized to $\mathcal{R}_\phi(\Delta = 0)$. For small nonlinearity, $\mathcal{R}_\phi(\Delta_{\text{opt}}) = \mathcal{R}_\phi(\Delta = 0)$, i.e., the optimal configuration is the resonant one. For larger U , however, a non-vanishing detuning improves $\mathcal{R}_\phi(\Delta_{\text{opt}})/\mathcal{R}_\phi(\Delta = 0)$ by several orders of magnitude.

Figures 7(b-c) display the behaviour of \mathcal{R}_ϕ as a function of Δ and U/η respectively for $\kappa_\phi/W = 10^{-5}$ and $\kappa_\phi/W = 10^{-2}$. The data show that, for $\Delta > 0$ and sizable nonlinearity, a parameter region with longer coherence times emerges.

In Appendix B we show this enhanced dephasing error suppression for experimentally viable parameters.

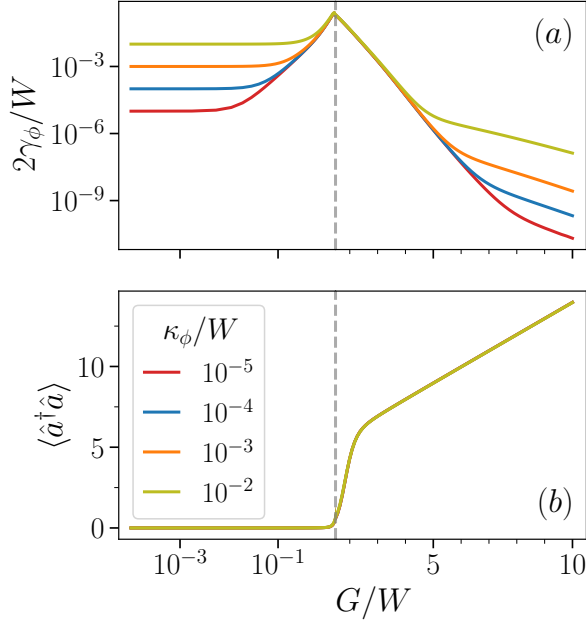


FIG. 6. (a) Phase-flip error rate γ_ϕ as a function of the amplitude of the two-photon driving amplitude G for a sub-optimal detuning choice $\Delta/W = 4$ and different values of κ_ϕ . The dashed vertical line indicates the value of G_c above which the exponential suppression of γ_ϕ is observed. (b) Average steady-state photon number (data computed for different values of κ_ϕ overlap).

V. EFFECT OF SINGLE PHOTON LOSS

We now study the effect of single-particle loss errors. As the strong \mathcal{Z}_2 symmetry is lost, the four-block-diagonal structure of the Liouvillian is replaced by a two-block-diagonal structure, $\mathcal{L} = \mathcal{L}_+ \oplus \mathcal{L}_-$ typical of the *weak* \mathcal{Z}_2 symmetry characterizing the system for finite κ_1 [see Fig. 1(c)]. The notion of diagonal and off-diagonal gap introduced in Sec. III A therefore no longer holds. Similarly to Eq. (4), we denote the eigenvalues of the weak \mathcal{Z}_2 symmetric Liouvillian as

$$\mathcal{L}_\mu \hat{\rho}_n^\mu = \lambda_n^\mu \hat{\rho}_n^\mu \quad \text{with} \quad -\text{Re}\{\lambda_n^\mu\} < -\text{Re}\{\lambda_{n+1}^\mu\}. \quad (24)$$

Within this picture, $\hat{\rho}_n^+$ ($\hat{\rho}_n^-$) can be expressed as a linear combination of the operators $\hat{\rho}_m^{++}$ and $\hat{\rho}_m^{--}$ ($\hat{\rho}_m^{+-}$ and $\hat{\rho}_m^{-+}$) defined in Eq. (4). As such, $\hat{\rho}_0^+$ and $\hat{\rho}_1^+$, describe the dynamics of the populations of the logical qubit, while $\hat{\rho}_0^-$ and $\hat{\rho}_1^-$ describe the dynamics of the coherences. The decay rates of populations and coherences are given by $\Lambda_n^\pm = -\text{Re}\{\lambda_n^\pm\}$. We remark that $\Lambda_0^+ = 0$ as \mathcal{L}_+ always hosts a steady state, while Λ_1^+ and $\Lambda_0^- \neq \Lambda_1^-$ are, in general, nonzero.

As anticipated above, under these conditions, the long-time dynamics of \hat{J}_x alone is no longer a valid measure of the loss of quantum information [53]. This is rendered manifest in Fig. 8 for the case of a purely dissipative

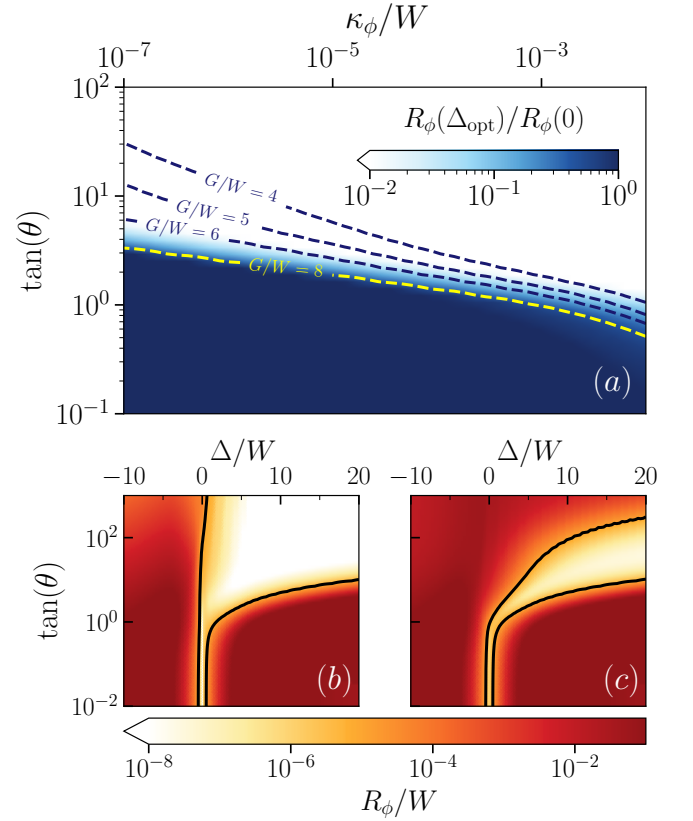


FIG. 7. (a) Normalized channel-fidelity decay rate $\mathcal{R}_\phi(\Delta_{\text{opt}})/\mathcal{R}_\phi(\Delta = 0)$ for several values of U/η and κ_ϕ/W . The dashed lines correspond to $\mathcal{R}_\phi(\Delta_{\text{opt}})/\mathcal{R}_\phi(\Delta = 0) = 1/2$, shown for increasing values of G/W . The color map is provided for the case $G/W = 8$. (b-c) Phase-flip error rate \mathcal{R}_ϕ as a function of Δ and U/η for $\kappa_\phi/W = 10^{-5}$ (b) and $\kappa_\phi/W = 10^{-2}$ (c).

($\theta = 0$, $G = 5$) cat qubit subject to $\kappa_\phi/W = 10^{-5}$ and $\kappa_1/W = 10^{-3}$, similar to that investigated in Ref. [24]. In Fig. 8(a) we display the decay rates Λ_n^\pm as a function of Δ , and mark with blue squares the values of $\Lambda_{0,1}^-$ governing the loss of coherence for $\Delta = 0$. While Λ_0^- is the decay rate governing the long-time dynamics, and is comparable to that obtained in the case $\kappa_1 = 0$, we observe that a second and faster decay rate is determined by $\Lambda_1^- \approx \max(\Lambda_1^+, \Lambda_0^-)$. This shows that κ_1 also determines the decay rate of the coherences, as $\Lambda_1^+ \propto \kappa_1 \langle \hat{a}^\dagger \hat{a} \rangle$. The presence of two time-scales characterizing the cat dynamics is also displayed by studying the time evolution of the qubit density matrix with initial condition $\hat{\rho}(0) = |+_L\rangle\langle+_L|$, and fitting $\langle \hat{J}_x \rangle$ with a double exponential function. The results are shown in Fig. 8(b). Finally, Fig. 8(c) displays the channel-fidelity decay rate \mathcal{R} , defined in Eq. (17), as a function of Δ for varying values of κ_1 . As argued above, this quantity is a more reliable measure of the qubit performance. We notice in passing, that the quantities \mathcal{R} and Λ_n^μ are linked. Indeed, it can be shown that $\mathcal{R}' = -\frac{1}{4} \sum_{n=0,1} \sum_{\mu=+,-} \Lambda_n^\mu$ approximates

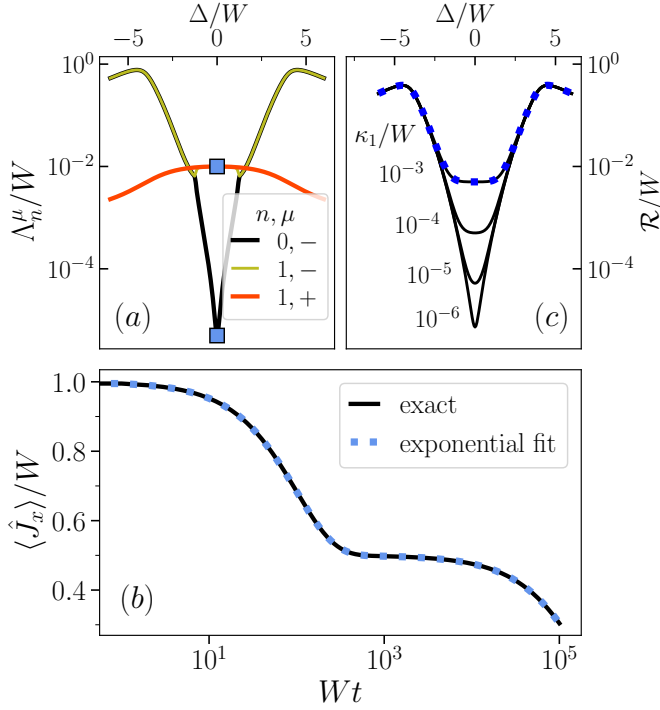


FIG. 8. (a) Low-lying Liouvillian spectrum Λ_n^μ . (b) The average $\langle \hat{J}_x \rangle$ vs time, as computed for $\kappa_\phi/W = 10^{-5}$ and $\kappa_1/W = 10^{-3}$. The numerical evolution of the master equation is shown as a solid line. We fit to the data the double exponential function $f(t) = c_1 \exp\{\Lambda_1 t\} + c_2 \exp\{\Lambda_2 t\}$ which is shown as superimposed dots. The extracted parameters coincide exactly with the time scales selected in panel (a) (blue squares). (c) Channel-fidelity decay rate \mathcal{R} . The blue dots describe the behaviour of \mathcal{R}' (defined in the main text) for $\kappa_1/W = 10^{-3}$.

\mathcal{R} to leading order in κ_1 [blue dots in Fig. 8(c)]. This indicates that κ_1 is just mixing the Liouvillian eigenstates of \mathcal{L}_0 without introducing sizable distortions.

We now focus on the slowest component of \mathcal{R} , i.e., Λ_1^+ , equivalent to the long-time decay rate of \hat{J}_x [24, 53]. If $\Delta = 0$, Λ_1^+ describes the rate at which $\hat{\rho} = |\alpha\rangle\langle\alpha| \rightarrow (|\alpha\rangle\langle\alpha| + |-\alpha\rangle\langle-\alpha|)/2$. We find a scaling in G analogous to that detailed in Fig. 5 even for $\kappa_1 \neq 0$ (not shown). As before, this scaling identifies the critical regime as the ideal configuration for large enough values of G . We conclude that the critical cat code is less affected by this error with respect to the standard cat, even in the presence of single photon loss. This makes it an ideal candidate for concatenation or repetition codes [69, 70].

In Fig. 9 we finally assess the combined effect of single-photon loss and dephasing on the encoded information as a function of Δ and for different choices of θ in Eq. (19). Panels (a-c) respectively display results obtained for $(\kappa_\phi/W, \kappa_1/W) = (10^{-5}, 10^{-3})$, $(10^{-4}, 10^{-4})$, $(10^{-3}, 10^{-5})$. As expected, for $U \gtrsim \eta$ a whole region of positive detuning opens up where information can be safely encoded. The effect of

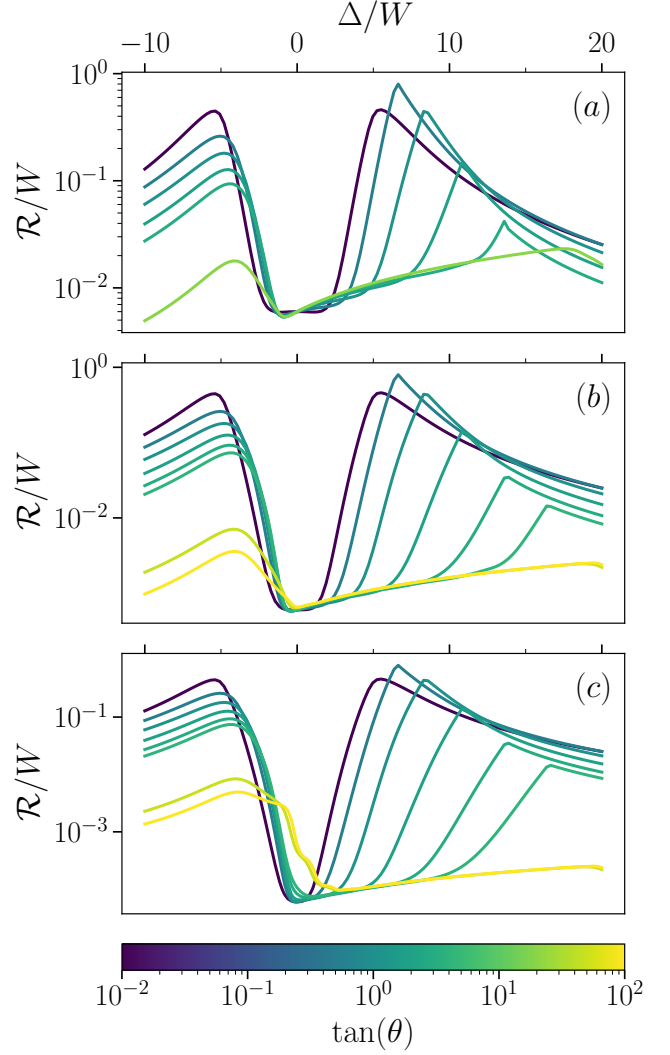


FIG. 9. channel-fidelity decay rate \mathcal{R} as a function of the detuning Δ for several values of θ and $(\kappa_\phi/W, \kappa_1/W) =$ (a) $(10^{-5}, 10^{-3})$, (b) $(10^{-4}, 10^{-4})$, and (c) $(10^{-3}, 10^{-5})$.

single-particle loss slightly hinders the advantage brought by criticality, in that $\mathcal{R}(\Delta \neq 0) \gtrsim \mathcal{R}(\Delta = 0)$. This effect is more pronounced whenever κ_1 is the dominant loss channel [Fig. 9(a)]. This analysis demonstrates that contrary to the Kerr cat qubit, even in the presence of sizable photon loss and dephasing, the critical cat code ensures a performance similar to that of a cat stabilized by autonomous dissipation, while still offering all the advantages of Hamiltonian confinement.

VI. CONCLUSIONS

We have investigated the properties of the Schrödinger's cat code in the whole range of regimes between the two limiting cases of dissipative [9, 17, 18] and Kerr [25–28] cat code. We have demonstrated that

operating the cat code at finite values of the detuning between the two-photon driving field and the cavity frequency dramatically increases the resilience of the cat qubit to dephasing. We have shown how this singular property is a consequence of a first-order dissipative phase transition that characterizes the system at finite detuning [34]. This critical cat code combines all the advantages of autonomous and Hamiltonian stabilization, without inheriting their main disadvantages. It also entails great robustness against random frequency shifts [31], which may arise from dispersive coupling to ancillary nonlinear elements. This feature solves an outstanding issue and paves the road to the design of efficient coupled cat qubits, both for two-qubit gates and for quantum error correction with repetition codes.

For the present study we have developed a highly reliable estimator of the qubit performance – the channel-fidelity decay rate – that is rooted in the spectral theory of Liouvillians, and can be straightforwardly applied to other bosonic qubits.

By studying the underlying lumped-element circuitual model, we have shown that the advantageous regime of the critical cat qubit lies within reach of state-of-the-art superconducting circuit platforms. Finally, we have explored protocols for one- and two-qubit gates, and shown that the critical dissipative regime achieves better accuracy over common one- and two-qubit gates.

Our analysis suggests that the largely unexplored parameter space of bosonic codes may still offer regions where specific properties of the code are enhanced. A more systematic investigation of the regimes of operation of all bosonic codes – possibly guided by automated optimization procedures [80] – may therefore lead to a significant improvement of such encoding schemes, and to a competitively efficient design of a bosonic quantum code architecture.

ACKNOWLEDGMENTS

We acknowledge useful discussions with Victor V. Albert, David Schlegel, Alexander Grimm, and Carlos Sánchez-Muñoz. This work was supported by the Swiss National Science Foundation through Project No. 200020_185015, and was conducted with the financial support of the EPFL Science Seed Fund 2021.

Appendix A: Characterization of the microscopic model

In this section we present the derivation behind Eq. (2) of the main text. Although we closely follow the arguments presented in the supplementary material of Ref. [17], we shall use this space to expand upon several of its aspects. We focus on the setup sketched in Fig. 10, following [9] and the experiments in Ref. [17, 18]. A highly coherent mode (storage) is implemented into a

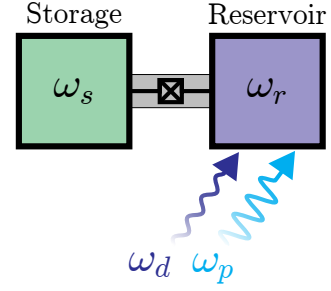


FIG. 10. Schematic representation of the microscopic model underlying Eq. (2). The reservoir mode at frequency ω_r is driven by two tones, the pump ω_p and the drive ω_d . The nonlinearity of the Josephson junction enables the pairwise exchange of photons between the reservoir and the storage, if the frequency matching condition $2\omega_s = \omega_p + \omega_d$ is met.

long-lived linear cavity and directly coupled the nonlinear mode (reservoir) of a trasmon with a much lower lifetime. The Hamiltonian of the coupled reservoir and storage modes reads

$$\mathcal{L}\hat{\rho} = -i[\hat{H}, \hat{\rho}] + \kappa_r \mathcal{D}[\hat{a}_r]\hat{\rho} + \kappa_s \mathcal{D}[\hat{a}_s]\hat{\rho}, \quad (\text{A1})$$

$$\begin{aligned} \hat{H} = & \sum_{m=r,s} \omega_m \hat{a}_m^\dagger \hat{a}_m - E_J \cos(\hat{\varphi}) + \\ & + 2 \text{Re}(\epsilon_p e^{-i\omega_p t} + \epsilon_d e^{-i\omega_d t}) (\hat{a}_r + \hat{a}_s^\dagger), \end{aligned} \quad (\text{A2})$$

$$\hat{\varphi} = \sum_{m=r,s} \varphi_m (\hat{a}_m + \hat{a}_m^\dagger), \quad (\text{A3})$$

where E_J denotes the Josephson energy, and $\omega_{p,s,r,d}$ are the pump, storage, reservoir, and drive frequencies, respectively. The phase $\hat{\varphi}$ across the junction is the sum of the phases $\varphi_m(\hat{a}_m^\dagger + \hat{a}_m)$ across each mode ($m = r, s$), with φ_m representing their zero point fluctuation. κ_m is the single photon loss rate of the modes with annihilation operator \hat{a}_m , while κ_ϕ describes the effects of coupled nonlinear modes such as the reservoir [11]. Pump and drive microwave tones, respectively with complex amplitudes ϵ_d , ϵ_p and frequencies ω_d , ω_p , are applied to the reservoir. We consider the regime in which the pump is strong and far off-resonant, while the drive is weak and close to resonance with respect to the reservoir mode. In particular, we have

$$\omega_d \simeq \omega_r \quad \text{and} \quad \epsilon_p \sim (\omega_p - \omega_r) \gg \frac{E_J}{24} \|\hat{\varphi}\|^4, \epsilon_d. \quad (\text{A4})$$

We move to a convenient frame via the unitary rotation $\hat{U} = \hat{U}_1 \hat{U}_2$, with

$$\begin{aligned} \hat{U}_1 = & \exp \left\{ it \left(\omega_d \hat{a}_r^\dagger \hat{a}_r + \frac{\omega_d + \omega_p}{2} \hat{a}_s^\dagger \hat{a}_s \right) \right\} \\ \hat{U}_2 = & \exp \left\{ \tilde{\xi}_p^*(t) \hat{a}_r - \tilde{\xi}_p(t) \hat{a}_r^\dagger \right\}. \end{aligned} \quad (\text{A5})$$

\hat{U}_2 removes the underlying photonic mean-field population rotating with frequency ω_p and supported by the strong pump ϵ_p . In fact, it can be decomposed as

$$\begin{aligned} U_2 &= \left(U_2^{(0)} \right)^\dagger U_2^{(1)} U_2^{(0)} \\ U_2^{(0)} &= \exp\{it\omega_p \hat{a}_r^\dagger \hat{a}_r\} \\ U_2^{(1)} &= \exp\{\xi_p^* \hat{a}_r - \xi_p \hat{a}_r^\dagger\}, \end{aligned} \quad (\text{A6})$$

i.e., a typical time-independent displacement transformation implemented in a frame rotating at ω_p . Here, $\tilde{\xi}_p(t) = \exp\{i\omega_p t\}\xi_p$, and

$$\xi_p = \frac{-i\epsilon_p}{\frac{\kappa_r}{2} + i(\omega_r - \omega_p)} \quad (\text{A7})$$

is the amplitude of the coherent steady state of the reservoir's isolated dynamics. \hat{U}_1 , on the other hand, is applied in hindsight of the phase matching condition $2\omega_s = \omega_p + \omega_r \approx \omega_p + \omega_d$ which, if met, establishes an approximate four-wave mixing channel within the Josephson Junction. This, as we shall see, allows for the parametric process converting two storage photons into one reservoir and one pump photon. Note that this series of transformations does not remove the time dependence from the Hamiltonian completely, but rather confines it within its nonlinear part. Indeed, in the rotated frame, the Hamiltonian reads

$$\begin{aligned} \tilde{H} &= (\omega_r - \omega_d) \hat{a}_r^\dagger \hat{a}_r + \left(\omega_s - \frac{\omega_p + \omega_d}{2} \right) \hat{a}_s^\dagger \hat{a}_s \\ &\quad + (\epsilon_d^* \hat{a}_r + \epsilon_d \hat{a}_r^\dagger) - E_J \cos \tilde{\varphi}, \end{aligned} \quad (\text{A8})$$

with

$$\begin{aligned} \tilde{\varphi} &= \sum_{m=r,s} \varphi_m \left(\tilde{a}_m + \tilde{a}_m^\dagger \right) + \left(\tilde{\xi}_p + \tilde{\xi}_p^* \right) \varphi_r \\ \tilde{a}_r &= \exp\{-it\omega_d\} \hat{a}_r \\ \tilde{a}_s &= \exp\left\{-it\frac{\omega_p + \omega_d}{2}\right\} \hat{a}_s. \end{aligned} \quad (\text{A9})$$

Finally, the cosine term is expanded up to fourth order as $\cos(\tilde{\varphi}) = 1 - \tilde{\varphi}^2/2 + \tilde{\varphi}^4/24 + \mathcal{O}(\tilde{\varphi}^6)$, and the resonant terms alone are retained.

Rotating wave approximation

Below we develop a general scheme to easily identify the resonant elements within $\tilde{\varphi}^n$. Let

$$\hat{A} = \sum_{i=1}^3 \hat{A}_i = \varphi_s \tilde{a}_s + \varphi_r \tilde{a}_r + \varphi_r \tilde{\xi}_p, \quad (\text{A10})$$

with

$$\hat{A}_1 = \varphi_s \tilde{a}_s, \quad \hat{A}_2 = \varphi_r \tilde{a}_r, \quad \hat{A}_3 = \varphi_r \tilde{\xi}_p, \quad (\text{A11})$$

and $\hat{Q} = \hat{A}^\dagger + \hat{A} = \tilde{\varphi}$. Although here we restrict to the case $i = 1, \dots, 3$, the generalization to a higher number of modes $i = 1, \dots, m \geq 3$ is immediate. Given that $C \equiv [\hat{A}, \hat{A}^\dagger] = \varphi_s^2 + \varphi_r^2 \in \mathbb{R}$, the non-commutative binomial theorem [81] can be used to write

$$\hat{Q}^n = \sum_{k=0}^{[n/2]} \frac{n!}{(n-2k)! k!} \left(\frac{C}{2} \right)^k : \hat{Q}^{n-2k} :, \quad (\text{A12})$$

with

$$: \hat{Q}^n : = \sum_{k=0}^n \binom{n}{k} (\hat{A}^\dagger)^k \hat{A}^{n-k} \quad (\text{A13})$$

representing the normal ordered expression of \hat{Q} [82, 83]. Moreover, the multinomial theorem provides us with an explicit expansion for the terms in the sum:

$$\hat{A}^n = \sum_{\Sigma \alpha = n} \binom{n}{\alpha} x^\alpha \quad \text{with} \quad \begin{cases} \alpha &= (\alpha_1, \dots, \alpha_3) \\ \Sigma \alpha &= \sum_i \alpha_i \\ x^\alpha &= \prod_i \hat{A}_i^{\alpha_i} \end{cases}. \quad (\text{A14})$$

The general term within the expansion of \hat{Q}^n , therefore, will be of the form

$$(\hat{A}^\dagger)^k \hat{A}^{n-k} = \sum_{\Sigma \alpha = k} \sum_{\Sigma \beta = n-k} \binom{k}{\alpha} \binom{n-k}{\beta} \prod_i (\hat{A}_i^\dagger)^{\alpha_i} \prod_j \hat{A}_j^{\beta_j} \quad (\text{A15})$$

The specifics of the problem under investigation enter in the rotation frequencies of the different \hat{A}_i s:

$$\begin{aligned} \hat{A}_1 &\sim \exp\left\{-i\frac{\omega_p + \omega_d}{2}t\right\} \\ \hat{A}_2 &\sim \exp\{-i\omega_d t\} \\ \hat{A}_3 &\sim \exp\{+i\omega_p t\}. \end{aligned} \quad (\text{A16})$$

The resonance condition, in this case, explicates in a set of two coupled equations for the coefficients in Eq. (A15)

$$\begin{cases} \frac{\alpha_1}{2} + \alpha_2 - \frac{\beta_1}{2} - \beta_2 = 0 \\ \frac{\alpha_1}{2} - \alpha_3 - \frac{\beta_1}{2} + \beta_3 = 0 \end{cases} \quad (\text{A17})$$

uniquely determining the possible values of $D_i = \alpha_i - \beta_i$. Equation (A17) provides therefore an algorithmic way of singling out the resonant terms within a symbolic evaluation of Eq. (A13). We immediately recognize that no resonant terms can exist within $: \hat{Q}^n :$ if $n \bmod 2 = 1$. Hereunder, we shall thus restrict our considerations to the case $n = 2m$ with $m \in \mathbb{N}_+$ and note that Eq. (A13) can be rewritten as

$$: \hat{Q}^n : \sim \binom{n}{m} (\hat{A}^\dagger)^m \hat{A}^m + \sum_{k=m+1}^{n-1} \binom{n}{k} \left[(\hat{A}^\dagger)^k \hat{A}^{n-k} + h.c \right] \quad (\text{A18})$$

where the symbol \sim is used to identify equality up to off-resonant contributions. Note that at this stage all terms of the expansion have been retained except for $k = 0$ and $k = n$ which are evidently off-resonant. Enforcing the conditions in Eq. (A17), the elements of the above sum simplify to

$$(\hat{A}^\dagger)^m \hat{A}^m \sim \sum_{\alpha_1=0}^m \sum_{\alpha_3=0}^{m-\alpha_1} C_{n,k}(\alpha_1, \alpha_3) (\hat{A}_1^\dagger)^{\alpha_1} \hat{A}_1^{\alpha_1} (\hat{A}_3^\dagger)^{\alpha_3} \hat{A}_3^{\alpha_3} (\hat{A}_2^\dagger)^{m-S_{13}} \hat{A}_2^{m-S_{13}} \quad (\text{A19})$$

and

$$(\hat{A}^\dagger)^k \hat{A}^{n-k} \sim \sum_{\alpha_1=2\zeta}^k \sum_{\alpha_3=\zeta}^{k-\alpha_1} C_{n,k}(\alpha_1, \alpha_3) (\hat{A}_1^\dagger)^{\alpha_1} (\hat{A}_3^\dagger)^{\alpha_3} (\hat{A}_2^\dagger)^{k-S_{13}} \hat{A}_1^{\alpha_1-2\zeta} \hat{A}_3^{\alpha_3-\zeta} \hat{A}_2^{k-S_{13}+\zeta}, \quad (\text{A20})$$

where $\zeta = k - m$, $S_{13} = \alpha_1 + \alpha_3$, and

$$C_{n,k}(\alpha_1, \alpha_3) = \binom{k}{\alpha_1 \ \alpha_3} \binom{n-k}{\alpha_1-2\zeta \ \alpha_3-\zeta}. \quad (\text{A21})$$

The terms of interest for the present discussion, \hat{Q}^2 and \hat{Q}^4 , are straightforwardly derived since the sums in Eq. (A18) contain at most one term:

$$:\hat{Q}^2: \sim 2 \sum_i \hat{A}_i^\dagger \hat{A}_i, \quad (\text{A22})$$

$$:\hat{Q}^4: \sim \left[12(\hat{A}_1^\dagger)^2 \hat{A}_3^\dagger \hat{A}_2 + h.c. \right] + 6 \sum_i (\hat{A}_i^\dagger)^2 \hat{A}_i^2 + 24 \sum_{i,j \neq i} \hat{A}_i^\dagger \hat{A}_i \hat{A}_j^\dagger \hat{A}_j. \quad (\text{A23})$$

Substitution into Eq. (A12), consequently yields

$$\begin{aligned} -E_J \cos \tilde{\varphi} &\approx \frac{E_J}{2} \tilde{\varphi}^2 - \frac{E_J}{24} \tilde{\varphi}^4 \\ &\sim \sum_{m=r,s} \omega_m^{(\text{eff})} \hat{a}_m^\dagger \hat{a}_m - \left[g_2 (\hat{a}_s^\dagger)^2 \hat{a}_r + h.c. \right] \\ &\quad - \sum_{m=r,s} \frac{U_m}{2} (\hat{a}_m^\dagger)^2 \hat{a}_m^2 - \chi_{rs} \hat{a}_s^\dagger \hat{a}_s \hat{a}_r^\dagger \hat{a}_r, \end{aligned} \quad (\text{A24})$$

where

$$U_m = \frac{E_J \varphi_m^4}{2}, \quad \chi_{rs} = E_J \varphi_s^2 \varphi_r^2, \quad g_2 = \frac{\chi_{rs} \xi_p^*}{2}, \quad (\text{A25})$$

with $m = s, r$, and

$$\omega_m^{\text{eff}} = E_J \varphi_m^2 \left(1 - \frac{C}{2} - \varphi_r^2 |\xi_p|^2 \right). \quad (\text{A26})$$

All in all, the Liouvillian under examination reads

$$\begin{aligned} \mathcal{L}\hat{\rho} &= -i \left[\tilde{\hat{H}}, \hat{\rho} \right] + \kappa_r \mathcal{D}[\hat{a}_r] \hat{\rho} + \kappa_s \mathcal{D}[\hat{a}_s] \hat{\rho} \\ \tilde{\hat{H}} &\approx \hat{H}_0 + \hat{H}_{\text{Kerr}} + \hat{H}_{\text{param}} \end{aligned} \quad (\text{A27})$$

with

$$\begin{aligned} \hat{H}_0 &= \sum_{m=r,s} \Delta_m \hat{a}_m^\dagger \hat{a}_m \\ \hat{H}_{\text{Kerr}} &= - \sum_{m=r,s} \frac{U_m}{2} (\hat{a}_m^\dagger)^2 \hat{a}_m^2 - \chi_{rs} \hat{a}_s^\dagger \hat{a}_s \hat{a}_r^\dagger \hat{a}_r \\ \hat{H}_{\text{param}} &= - \left[\left(g_2 (\hat{a}_s^\dagger)^2 + \epsilon_d^* \right) \hat{a}_r + h.c. \right], \end{aligned} \quad (\text{A28})$$

and

$$\begin{aligned} \Delta_s &= \omega_s + \omega_s^{\text{eff}} - \frac{\omega_p + \omega_d}{2} \\ \Delta_r &= \omega_r + \omega_r^{\text{eff}} - \omega_d. \end{aligned} \quad (\text{A29})$$

Here, \hat{H}_0 incorporates all frequency shifts induced by the normal ordering of the nonlinear terms and the driving tones alike, \hat{H}_{Kerr} all self-Kerr and cross-Kerr coupling terms, and \hat{H}_{param} the seed for the degenerate parametric driving of the storage mode.

Through Eqs. (A19) and (A20), one can also easily evaluate the leading correction to such approximation. The only missing quantity for its evaluation is in fact $:\hat{Q}^6:$, which reads

$$\begin{aligned} :\hat{Q}^6: &\sim \left[180(\hat{A}_1^\dagger)^2 \hat{A}_2^\dagger \hat{A}_3 \hat{A}_2^2 + 180(\hat{A}_1^\dagger)^2 (\hat{A}_3^\dagger)^2 \hat{A}_2 \hat{A}_3 \right. \\ &\quad \left. + 120(\hat{A}_1^\dagger)^3 \hat{A}_3^\dagger \hat{A}_1 \hat{A}_2 + h.c. \right] + 720 \prod_i \hat{A}_i^\dagger \hat{A}_i \\ &\quad + 20 \sum_i (\hat{A}_i^\dagger)^3 \hat{A}_i^3 + 180 \sum_{i,j \neq i} (\hat{A}_i^\dagger)^2 \hat{A}_i^2 \hat{A}_j^\dagger \hat{A}_j \end{aligned} \quad (\text{A30})$$

Adiabatic elimination of the reservoir mode

Assuming the reservoir mode to be strongly damped, we look for a joint density matrix of the form

$$\begin{aligned} \hat{\rho}_{sr} &= \hat{\rho}_{00} |0\rangle\langle 0| + \delta (\hat{\rho}_{01} |0\rangle\langle 1| + \hat{\rho}_{10} |1\rangle\langle 0|) \\ &\quad + \delta^2 (\hat{\rho}_{11} |1\rangle\langle 1| + \hat{\rho}_{20} |2\rangle\langle 0| + \hat{\rho}_{02} |0\rangle\langle 2|), \end{aligned} \quad (\text{A31})$$

where $\delta \ll 1$ is a small expansion parameter and $\hat{\rho}_{mn}$ are reduced density matrices acting on the storage Hilbert space. Retaining only up to second order terms in δ within the equations of motion stemming from such an ansatz, we can adiabatically eliminate the reservoir mode in favour of a master equation describing the dynamics of the reduced density matrix $\hat{\rho}_s \approx \text{Tr}_r \{ \hat{\rho}_{sr} \} = \hat{\rho}_{00} + \delta^2 \hat{\rho}_{11}$ of the storage mode alone. In particular, we consider g_2 ,

$\epsilon_d, U_s, \chi_{rs}, \Delta_s, \kappa_s \sim \delta \kappa_r$. Using that $\partial_t \hat{\rho}_{ij} = \langle i | \mathcal{L} \hat{\rho}_{rs} | j \rangle$, we have

$$\begin{aligned} \frac{\partial \hat{\rho}_{00}}{\kappa_r \partial t} = & -\frac{i}{\kappa_r} [\{\Delta_s \hat{a}_s^\dagger \hat{a}_s - U_s (\hat{a}_s^\dagger)^2 \hat{a}_s^2\}, \hat{\rho}_{00}] + \frac{\kappa_s}{\kappa_r} \mathcal{D}[\hat{a}_s] \hat{\rho}_{00} \\ & + \delta^2 [\hat{\rho}_{11} - i(\hat{A}^\dagger \hat{\rho}_{10} - \hat{\rho}_{01} \hat{A})] + \mathcal{O}(\delta^3) \end{aligned} \quad (\text{A32})$$

$$\frac{\partial \hat{\rho}_{10}}{\kappa_r \partial t} = -\left(\frac{1}{2} + i\frac{\Delta_r}{\kappa_r}\right) \hat{\rho}_{10} - i\hat{A} \hat{\rho}_{00} + \mathcal{O}(\delta) \quad (\text{A33})$$

$$\frac{\partial \hat{\rho}_{11}}{\kappa_r \partial t} = -i(\hat{A} \hat{\rho}_{01} - \hat{\rho}_{10} \hat{A}^\dagger) - \hat{\rho}_{11} + \mathcal{O}(\delta), \quad (\text{A34})$$

where $\hat{A} = \frac{1}{\delta \kappa_r} (g_2 \hat{a}_s^2 + \epsilon_d^*) \sim \mathcal{O}(1)$. At this point the adiabatic approximation consists in setting $\partial_t \hat{\rho}_{01} = \partial_t \hat{\rho}_{11} = 0$ and using the expression for $\hat{\rho}_{01}$ and $\hat{\rho}_{11}$ resulting from the homogeneous solutions to Eqs. (A33) and (A34), as well as Eq. (A32), to obtain

$$\begin{aligned} \frac{\partial \hat{\rho}_s}{\partial t} = & -i[\Delta_s \hat{a}_s^\dagger \hat{a}_s - U_s (\hat{a}_s^\dagger)^2 \hat{a}_s^2, \hat{\rho}_s] + \kappa_s \mathcal{D}[\hat{a}_s] \hat{\rho}_s \\ & - \delta^2 \kappa_r \left\{ \Gamma (\hat{A}^\dagger \hat{A} \hat{\rho}_s - \hat{A} \hat{\rho}_s \hat{A}^\dagger) + h.c. \right\}, \end{aligned} \quad (\text{A35})$$

where $\Gamma^{-1} = 1/2 - i\Delta_r/\kappa_r$. Through some rearranging, the above can be cast into the common form $\hat{\rho}_s = \mathcal{L}_s \hat{\rho}_s$ with

$$\begin{aligned} \mathcal{L}_s \hat{\rho}_s = & -i[\hat{H}_s, \hat{\rho}_s] + \{\eta \mathcal{D}[\hat{a}_s^2] + \kappa_s \mathcal{D}[\hat{a}_s]\} \hat{\rho}_s, \\ \hat{H}_s = & \Delta_s \hat{a}_s^\dagger \hat{a}_s + \frac{G^*}{2} \hat{a}_s^2 + \frac{G}{2} (\hat{a}_s^\dagger)^2 - \frac{U_s}{2} (\hat{a}_s^\dagger)^2 \hat{a}_s^2. \end{aligned} \quad (\text{A36})$$

and

$$G = \frac{-2i\Gamma\epsilon_d g_2}{\kappa_r}, \quad \eta = \frac{2\text{Re}\{\Gamma\}|g_2|^2}{\kappa_r}. \quad (\text{A37})$$

For the case $\Delta_r = 0$, the latter expressions simplify to

$$G = \frac{-4ig_2\epsilon_d}{\kappa_r}, \quad \eta = \frac{4|g_2|^2}{\kappa_r}. \quad (\text{A38})$$

Label	U/η	G/η	χ_{rs}/η	η [MHz]
<i>a</i>	0.016	4.81	5.46	1.17
<i>b</i>	1	10.7	4.91	4.50
<i>c</i>	2	14.1	6.43	2.15
<i>d</i>	3	19.9	9.11	1.07
<i>e</i>	4	23.9	10.7	0.75
<i>f</i>	5	29.1	13.3	0.50

TABLE I. A possible parameter choice leading to the configurations examined below. The first row reflects the choice of parameters adopted in Ref. [18], where the Kerr nonlinearity is minimal. The remaining configurations explore different choices for the Kerr nonlinearity, while enforcing the constraint of immediate experimental viability. In particular, we set the maximal dissipation rate of the reservoir cavity to $\kappa_r \approx 100$ MHz. For all sets, we take $|\xi_p| \approx 1$.

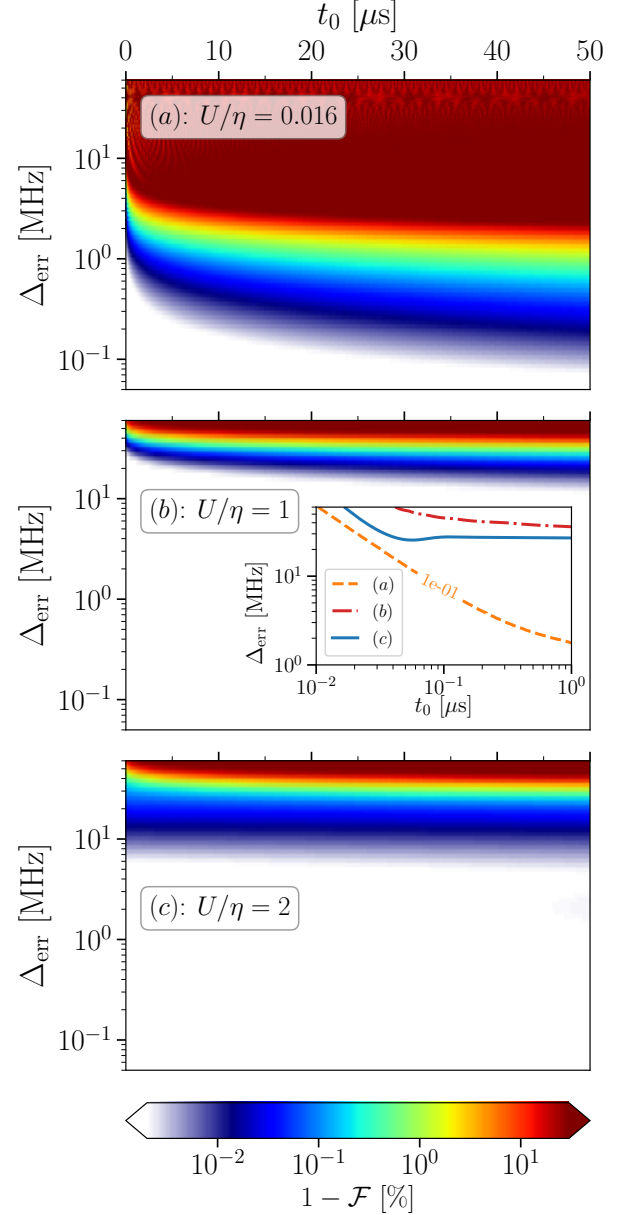


FIG. 11. Quantum information recovery from frequency errors. (a,b,c) Infidelity between the initial state $|+_L\rangle$ and the final state obtained from the recovery procedure detailed in the text. The three panels correspond respectively to the three parameter sets (a-c) in Table I. The inset details the behaviour at small time t_0 through contour lines at $1 - \mathcal{F} = 0.1\%$. For all sets of parameters, we set $\Delta = 0$ at $t = 0$.

Appendix B: Experimental parameters

Here we explore a realistic implementation of the critical cat code, by enforcing the microscopic constraints derived above. In Tab. I, we propose a choice of six sets of values of the physical parameters fulfilling these conditions. The first set of values coincides with the ex-

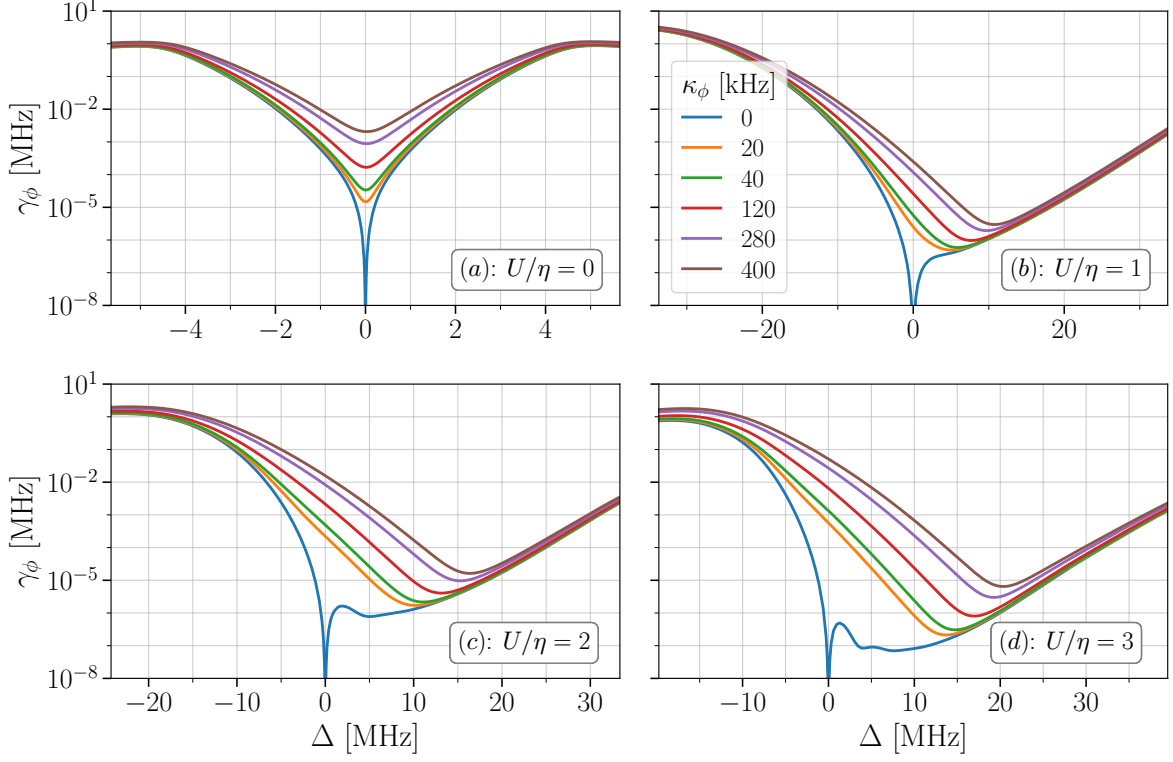


FIG. 12. Phase-flip error rates γ_ϕ as a function of the detuning Δ for the sets of parameters in Tab. I(a-d). Different values of the dephasing rate κ_ϕ were explored around those suggested by Eq. (B2).

perimental regime of Ref. [18], and is characterized by a vanishing nonlinearity. The remaining five rows correspond to values of the dimensionless nonlinearity U/η several orders of magnitude larger than those found in, e.g., Ref. [18].

We notice that the values in Tab. I(b) and (c) also lead to larger values of η than in the conventional case in Tab. I(a). This entails a faster performance of the logical operations on the CDC qubit, as argued in App. C, where we show that a universal set of gates for the CDC is identical to that of the conventional cat [9].

Recovery from frequency shifts

We perform an examination analogous to that carried out in Sec. III C for the parameters in Tab. I(a-c). Contrarily to Fig. 3, in Fig. 11 we fix $\Delta = 0$ and explore different quenching times t_0 and different spurious detuning strengths Δ_{err} . This time we show the infidelity $1 - \mathcal{F}$ between the initial and final states computed with

$$\mathcal{F}(\hat{Q}(0), \hat{Q}(t)) = \text{Tr}\left\{\hat{Q}(0)\hat{Q}(t)\right\} + 2\sqrt{\det[\hat{Q}(0)]\det[\hat{Q}(t)]} \quad (\text{B1})$$

Figure 11(a) shows the result for the weakly nonlinear regime in row (a) of Tab. I. Here, moderate values of

Δ_{err} induce a rapid loss of fidelity, constraining the performance of the code to a narrow region of values around $\Delta = 0$, hence confirming the analysis of the main text. Figs. 11(b) and 11(c), display the results of the same analysis, respectively for the parameters in rows (b) and (c) of Tab. I. Here, the system is clearly more resilient to frequency shifts. In particular, a sizeable loss of fidelity only occurs at significantly higher values of Δ_{err} , and at a much lower rate in terms of t_0 . These conclusions also hold at very short times, as shown in the inset of Fig. 11(b), where infidelity isolines are plotted for the choices of parameters.

Effect of dephasing

In a typical experimental setup, dephasing of the storage cavity is mostly due to random fluctuations associated to the thermal occupation of other dispersively coupled circuitual elements, such as Josephson junctions or the reservoir cavity [11, 18, 84]. Calling $\bar{n}_{\text{th}} \ll 1$ the average thermal occupation of coupled elements, the induced dephasing rate in the Markov approximation is then given by [85]

$$\kappa_\phi \approx \bar{n}_{\text{th}} \frac{\kappa_r \chi_{rs}^2}{\kappa_r^2 + \chi_{rs}^2}, \quad (\text{B2})$$

where κ_r and χ_{rs} respectively denote the loss rate and the dispersive coupling strength of the coupled elements. For this analysis, we assume the same thermal occupation $\bar{n}_{th} = 0.04$ for all parameter settings in Tab. I. In this case, Eq. (B2) predicts comparable values of κ_ϕ for all configurations. In Fig. 12, the qubit phase-flip rate γ_ϕ is displayed for dephasing rates $\kappa_\phi/\bar{n}_{th} \in [0.5, 10]$ MHz, and for the parameter sets in Tab. I(a-d). The finite value of κ_ϕ results in $\gamma_\phi \neq 0$ for all choices of U and Δ . By comparing the results in Fig. 12(b-d) to Fig. 12(a), a broad range of values of the detuning clearly emerges, where the strongly Kerr nonlinear cases largely outperform the weakly Kerr nonlinear one for all values of κ_ϕ . We confirm, therefore, that under the microscopic constraints imposed by the experimental setup, operating the qubit in the regime of large nonlinearity entails a better protection of quantum information against dephasing.

Appendix C: One- and two-qubit gates

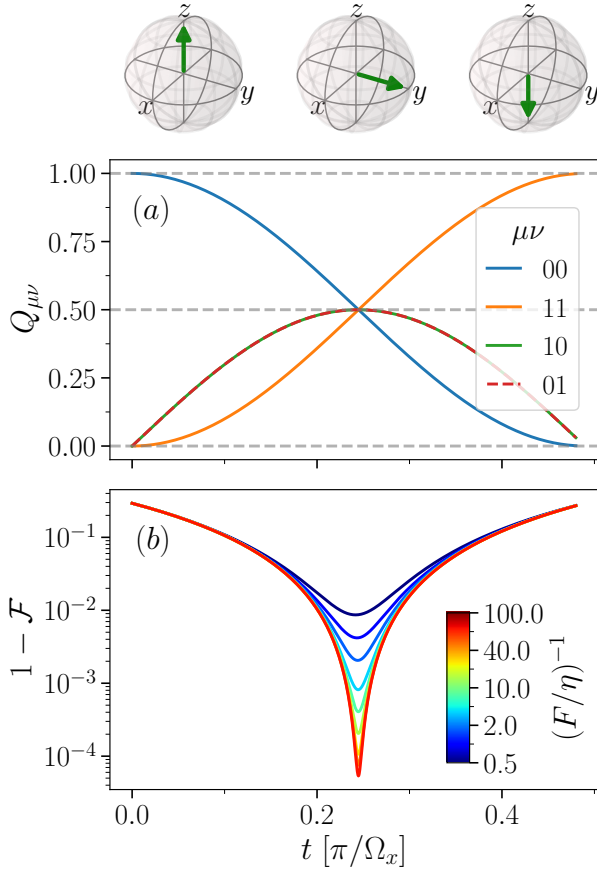


FIG. 13. Single qubit X -gate on a critical dissipative system. (a) Evolution of the populations and coherences of the qubit's matrix \hat{Q} under the action of \mathcal{L}' . (b) Infidelity between the expected state $|+_L\rangle$ and the numerical simulation. All quantities were computed for the settings in row (f) of Tab. I and $\Delta = G$.

We first focus on performing Rabi oscillations of an arbitrary angle θ around the x -axis of the Bloch sphere, as illustrated in Fig. 13. Borrowing from [9], the simplest Hamiltonian ensuring this gate operation is that of a linear resonant drive of the storage mode: $\hat{H}_X = F(\hat{a} + \hat{a}^\dagger)$. Indeed, the density operators $|0_L\rangle\langle 0_L|$ and $|1_L\rangle\langle 1_L|$ belong respectively to the $++$ and $--$ diagonal parity manifolds, which can be connected by single-photon exchange. The driving field amplitude F should then be chosen to be much smaller than W , in order to minimize the diffusion out of the steady state manifold, induced by higher order terms in the gate operation [9]. The effective frequency (period) $\Omega_X = 2F \text{Re}\{\alpha\}$ ($T_X = \pi/\Omega_X$) of the Rabi oscillation is determined by setting $\Delta = 0$ and applying the Hamiltonian \hat{H}_X to the pure cat states $|\mathcal{C}_\alpha^\pm\rangle$. We numerically verify that the same value of Ω_X approximately holds for all configurations explored in Table I(b-f). In Fig. 13(a), the evolution of the density matrix elements $Q_{\mu\nu}$ ($\mu, \nu \in \{+, -\}$) under the action of Hamiltonian \hat{H}_X are plotted over half a period of the Rabi oscillation. For these data, we chose the parameter settings of Tab. I(f), and set $\Delta = G$ and $F/\eta = 1/40$. Figure 13(b) displays the computed infidelity [c.f. Eq. (B1)] between the expected state $|+_L\rangle$ and the actual outcome of the gate operation $\hat{\rho}(T_X/4) = \exp\{\mathcal{L}' T_X/4\} |0_L\rangle$, where $\mathcal{L}'\hat{\rho} = \mathcal{L}_0\hat{\rho} - i[\hat{H}_X, \hat{\rho}]$. The two plots clearly indicate that the gate operation can be executed on the critical dissipative cat code. In particular, the accuracy of the operation increases with $(F/W)^{-1}$.

In the presence of single-photon loss with rate κ and dephasing with rate κ_ϕ , an upper bound to the ratio $(F/W)^{-1}$ arises, as increasing this quantity slows down the gate operation making it more vulnerable to photon-loss and dephasing errors. To gauge the efficiency at which X operations can be performed in the presence of photon loss and dissipation, we set $\kappa_1 = \kappa_\phi = 1$ kHz,

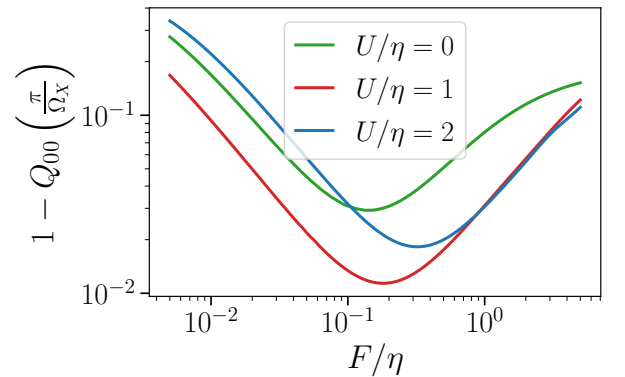


FIG. 14. Separation between the initial state $|0_L\rangle$ and the final state $\hat{\rho}(\pi/\Omega_x)$ following a full Rabi oscillation (c.f. Fig. 13). We consider the parameter configurations of Table I(a-c) and operate them respectively at $\Delta/G = 0, 0.40, 0.68$. We set $\kappa_1 = \kappa_\phi = 1$ kHz.

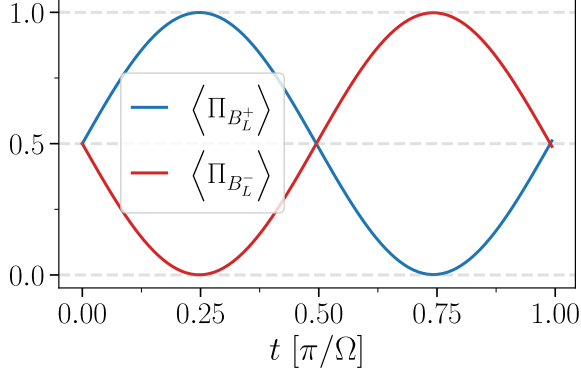


FIG. 15. Two-qubit XX -gate on a critical dissipative system. We display the time evolution of the occupations of the states $|B_L^\pm\rangle$ under the Liouvillian \mathcal{L}' (see text). We recall that the physical states encoding $|B_L^\pm\rangle$ are mixed, see Eq. (7).

and study the parameter settings in rows (a-c) of Tab. (I). For each setting, the gate operation is performed onto the manifold stabilized by the respective parameters. Hence, the logical code words $|0_L\rangle$ and $|1_L\rangle$ denote different states for each of the three settings.

We initialize the system in the state $|0_L\rangle$, perform a full Rabi oscillation, and evaluate the overlap between the final and initial states. The results are shown in Fig. 14 as a function of F/η . For both Kerr nonlinear configurations [Tab. I(b,c)] we observe a significant improvement in the performance of the X gate with respect to the $U = 0$ case [Tab. I(a)].

In the same way in which the Hilbert space of two physical qubit acquires a tensor product structure, so do the logical qubits encoded in the NS. In fact, one can define the two qubit matrix $Q^{(2)}$ using the conserved quantities of the single qubit as

$$Q_{\mu\mu',\nu\nu'}^{(2)} = \text{Tr}\left\{\hat{\rho} \left(\hat{J}_0^{\mu\nu}\right)^\dagger \otimes \left(\hat{J}_0^{\mu'\nu'}\right)^\dagger\right\}. \quad (\text{C1})$$

Within this logical Hilbert space, we can describe the effects of entangling gates. For instance, as a witness of entanglement generation upon the action of $\hat{\sigma}_L^x \otimes \hat{\sigma}_L^x$, we consider

$$\langle \hat{\Pi}_{B_L^\pm} \rangle = \text{Tr}\left\{\hat{\Pi}_{B_L^\pm} Q^{(2)}\right\}, \quad (\text{C2})$$

where $\hat{\Pi}_{B_L^\pm}$ is the projector on the logical Bell states defined as

$$|B_L^\pm\rangle = \frac{|0_L\rangle \otimes |0_L\rangle \pm |1_L\rangle \otimes |1_L\rangle}{\sqrt{2}}. \quad (\text{C3})$$

Similarly to the conventional cat qubit, an entangling Hamiltonian of this form between two interacting cat qubits is realized by the photon hopping Hamiltonian

$$\hat{H}_{XX} = J \left(\hat{a}_1 \hat{a}_2^\dagger + \hat{a}_1^\dagger \hat{a}_2 \right), \quad (\text{C4})$$

where a_1 and a_2 are the annihilation operators of the storage modes of the two cat qubits.

Within the effective qubit manifold, it can be shown that this Hamiltonian is approximately recast as [9]

$$\hat{H}_{XX} \simeq \Omega_{XX} \hat{\sigma}_1^x \otimes \hat{\sigma}_2^x, \quad (\text{C5})$$

where $\Omega_{XX} = 2J|\alpha_1\alpha_2|$. Similarly to the one qubit gate, this approximation is exact in the limit $J/\eta \rightarrow 0$.

We provide here evidence of the effectiveness of this protocol, when applied to the parameter settings in row (c) of Tab. I. We initialize the system to the logical state $|0_L\rangle \otimes |0_L\rangle$, and let it evolve under the action of the Hamiltonian in Eq. (C4). Figure 15 displays the evolution of the projection $\langle \hat{\Pi}_{B_L^\pm} \rangle(t)$ under the Liouvillian $\mathcal{L}'\hat{\rho} = \mathcal{L}_0\hat{\rho} - i[\hat{H}_{XX}, \hat{\rho}]$. Over time, the system oscillates between the Bell states in Eq. (C3). In the ideal case, in the absence of single-photon loss and dephasing processes, the gate accuracy can be increased at will by decreasing the ratio J/η . Again, dephasing induced by the finite off-diagonal gap Λ^{+-} and single photon loss will set a lower bound on J .

-
- [1] D. A. Lidar and T. A. Brun, eds., *Quantum Error Correction* (Cambridge University Press, Cambridge, 2013).
 - [2] S. Haroche and J.-M. Raimond, *Exploring the Quantum: Atoms, Cavities, and Photons* (Oxford University Press, Oxford, 2013).
 - [3] J. Preskill, *Quantum Computing in the NISQ Era and Beyond*, *Quantum* **2**, 79 (2018).
 - [4] H.-P. Breuer and F. Petruccione, *The Theory of Open Quantum Systems* (Oxford University Press, Oxford, 2007).
 - [5] M. A. Nielsen and I. L. Chuang, *Quantum Computation and Quantum Information: 10th Anniversary Edition*, tenth ed. (Cambridge University Press, USA, 2011).
 - [6] E. T. Campbell, B. M. Terhal and C. Vuillot, *Roads towards Fault-Tolerant Universal Quantum Computation*, *Nature* **549**, 172 (2017).
 - [7] B. M. Terhal, *Quantum Error Correction for Quantum Memories*, *Rev. Mod. Phys.* **87**, 307 (2015).
 - [8] D. Gottesman, A. Kitaev and J. Preskill, *Encoding a Qubit in an Oscillator*, *Phys. Rev. A* **64**, 012310 (2001).
 - [9] M. Mirrahimi, Z. Leghtas, V. V. Albert, S. Touzard, R. J. Schoelkopf, L. Jiang and M. H. Devoret, *Dynamically Protected Cat-Qubits: A New Paradigm for Universal Quantum Computation*, *New J. Phys.* **16**, 045014 (2014).
 - [10] W. Cai, Y. Ma, W. Wang, C.-L. Zou and L. Sun, *Bosonic Quantum Error Correction Codes in Superconducting Quantum Circuits*, *Fundamental Research* **1**, 50 (2021).
 - [11] A. Joshi, K. Noh and Y. Y. Gao, *Quantum Information Processing with Bosonic Qubits in Circuit QED*, *Quan-*

- tum Sci. Technol. **6**, 033001 (2021).
- [12] B. M. Terhal, J. Conrad and C. Vuillot, *Towards Scalable Bosonic Quantum Error Correction*, [Quantum Sci. Technol.](#) **5**, 043001 (2020).
 - [13] E. Knill, R. Laflamme and L. Viola, *Theory of Quantum Error Correction for General Noise*, [Phys. Rev. Lett.](#) **84**, 2525 (2000).
 - [14] M. H. Michael, M. Silveri, R. T. Brierley, V. V. Albert, J. Salmilehto, L. Jiang and S. M. Girvin, *New Class of Quantum Error-Correcting Codes for a Bosonic Mode*, [Phys. Rev. X](#) **6**, 031006 (2016).
 - [15] V. V. Albert, K. Noh, K. Duivenvoorden, D. J. Young, R. T. Brierley, P. Reinhold, C. Vuillot, L. Li, C. Shen, S. M. Girvin, B. M. Terhal and L. Jiang, *Performance and Structure of Single-Mode Bosonic Codes*, [Phys. Rev. A](#) **97**, 032346 (2018).
 - [16] L. Gilles, B. M. Garraway and P. L. Knight, *Generation of Nonclassical Light by Dissipative Two-Photon Processes*, [Phys. Rev. A](#) **49**, 2785 (1994).
 - [17] Z. Leghtas, S. Touzard, I. M. Pop, A. Kou, B. Vlastakis, A. Petrenko, K. M. Sliwa, A. Narla, S. Shankar, M. J. Hatridge, M. Reagor, L. Frunzio, R. J. Schoelkopf, M. Mirrahimi and M. H. Devoret, *Confining the State of Light to a Quantum Manifold by Engineered Two-Photon Loss*, [Science](#) **347**, 853 (2015).
 - [18] S. Touzard, A. Grimm, Z. Leghtas, S. O. Mundhada, P. Reinhold, C. Axline, M. Reagor, K. Chou, J. Blumoff, K. M. Sliwa, S. Shankar, L. Frunzio, R. J. Schoelkopf, M. Mirrahimi and M. H. Devoret, *Coherent Oscillations inside a Quantum Manifold Stabilized by Dissipation*, [Phys. Rev. X](#) **8**, 021005 (2018).
 - [19] Q. Xu, J. K. Iverson, F. G. S. L. Brandão and L. Jiang, *Engineering Fast Bias-Preserving Gates on Stabilized Cat Qubits*, [Phys. Rev. Research](#) **4**, 013082 (2022).
 - [20] H. Goto, *Universal Quantum Computation with a Nonlinear Oscillator Network*, [Phys. Rev. A](#) **93**, 050301 (2016).
 - [21] P. T. Cochrane, G. J. Milburn and W. J. Munro, *Macroscopically Distinct Quantum-Superposition States as a Bosonic Code for Amplitude Damping*, [Phys. Rev. A](#) **59**, 2631 (1999).
 - [22] V. V. Albert, B. Bradlyn, M. Fraas and L. Jiang, *Geometry and Response of Lindbladians*, [Phys. Rev. X](#) **6**, 041031 (2016).
 - [23] V. V. Albert, *Lindbladians with Multiple Steady States: Theory and Applications* (2018), [arXiv:1802.00010](#).
 - [24] R. Gautier, A. Sarlette and M. Mirrahimi, *Combined Dissipative and Hamiltonian Confinement of Cat Qubits*, [PRX Quantum](#) **3**, 020339 (2022).
 - [25] S. Puri, S. Boutin and A. Blais, *Engineering the Quantum States of Light in a Kerr-nonlinear Resonator by Two-Photon Driving*, [npj Quantum Inf](#) **3**, 1 (2017).
 - [26] S. Puri, A. Grimm, P. Campagne-Ibarcq, A. Eickbusch, K. Noh, G. Roberts, L. Jiang, M. Mirrahimi, M. H. Devoret and S. M. Girvin, *Stabilized Cat in a Driven Nonlinear Cavity: A Fault-Tolerant Error Syndrome Detector*, [Phys. Rev. X](#) **9**, 041009 (2019).
 - [27] S. Puri, L. St-Jean, J. A. Gross, A. Grimm, N. E. Frattini, P. S. Iyer, A. Krishna, S. Touzard, L. Jiang, A. Blais, S. T. Flammia and S. M. Girvin, *Bias-Preserving Gates with Stabilized Cat Qubits*, [Science Advances](#) **6**, eaay5901 (2020).
 - [28] A. Grimm, N. E. Frattini, S. Puri, S. O. Mundhada, S. Touzard, M. Mirrahimi, S. M. Girvin, S. Shankar and M. H. Devoret, *Stabilization and Operation of a Kerr-cat Qubit*, [Nature](#) **584**, 205 (2020).
 - [29] D. Ruiz, R. Gautier, J. Guillaud and M. Mirrahimi, *Two-Photon Driven Kerr Quantum Oscillator with Multiple Spectral Degeneracies* (2022), [arXiv:2211.03689](#).
 - [30] N. E. Frattini, R. G. Cortiñas, J. Venkatraman, X. Xiao, Q. Su, C. U. Lei, B. J. Chapman, V. R. Joshi, S. M. Girvin, R. J. Schoelkopf, S. Puri and M. H. Devoret, *The Squeezed Kerr Oscillator: Spectral Kissing and Phase-Flip Robustness* (2022), [arXiv:2209.03934](#).
 - [31] S. Lieu, R. Belyansky, J. T. Young, R. Lundgren, V. V. Albert and A. V. Gorshkov, *Symmetry Breaking and Error Correction in Open Quantum Systems*, [Phys. Rev. Lett.](#) **125**, 240405 (2020).
 - [32] F. Minganti, A. Biella, N. Bartolo and C. Ciuti, *Spectral Theory of Liouvillians for Dissipative Phase Transitions*, [Phys. Rev. A](#) **98**, 042118 (2018).
 - [33] M. Aspelmeyer, T. J. Kippenberg and F. Marquardt, *Cavity Optomechanics*, [Rev. Mod. Phys.](#) **86**, 1391 (2014).
 - [34] N. Bartolo, F. Minganti, W. Casteels and C. Ciuti, *Exact Steady State of a Kerr Resonator with One- and Two-Photon Driving and Dissipation: Controllable Wigner-function Multimodality and Dissipative Phase Transitions*, [Phys. Rev. A](#) **94**, 033841 (2016).
 - [35] A. Biella, F. Storme, J. Lebreuilly, D. Rossini, R. Fazio, I. Carusotto and C. Ciuti, *Phase Diagram of Incoherently Driven Strongly Correlated Photonic Lattices*, [Phys. Rev. A](#) **96**, 023839 (2017).
 - [36] H. J. Carmichael, *Breakdown of Photon Blockade: A Dissipative Quantum Phase Transition in Zero Dimensions*, [Phys. Rev. X](#) **5**, 031028 (2015).
 - [37] W. Casteels, R. Fazio and C. Ciuti, *Critical Dynamical Properties of a First-Order Dissipative Phase Transition*, [Phys. Rev. A](#) **95**, 012128 (2017).
 - [38] W. Casteels and C. Ciuti, *Quantum Entanglement in the Spatial-Symmetry-Breaking Phase Transition of a Driven-Dissipative Bose-Hubbard Dimer*, [Phys. Rev. A](#) **95**, 013812 (2017).
 - [39] T. Fink, A. Schade, S. Höfling, C. Schneider and A. Imamoglu, *Signatures of a Dissipative Phase Transition in Photon Correlation Measurements*, [Nature Phys](#) **14**, 365 (2018).
 - [40] M. Fitzpatrick, N. M. Sundaresan, A. C. Y. Li, J. Koch and A. A. Houck, *Observation of a Dissipative Phase Transition in a One-Dimensional Circuit QED Lattice*, [Phys. Rev. X](#) **7**, 011016 (2017).
 - [41] E. M. Kessler, G. Giedke, A. Imamoglu, S. F. Yelin, M. D. Lukin and J. I. Cirac, *Dissipative Phase Transition in a Central Spin System*, [Phys. Rev. A](#) **86**, 012116 (2012).
 - [42] F. Minganti, I. I. Arkhipov, A. Miranowicz and F. Nori, *Liouvillian Spectral Collapse in the Scully-Lamb Laser Model*, [Phys. Rev. Research](#) **3**, 043197 (2021).
 - [43] V. R. Overbeck, M. F. Maghrebi, A. V. Gorshkov and H. Weimer, *Multicritical Behavior in Dissipative Ising Models*, [Phys. Rev. A](#) **95**, 042133 (2017).
 - [44] R. Rota, F. Storme, N. Bartolo, R. Fazio and C. Ciuti, *Critical Behavior of Dissipative Two-Dimensional Spin Lattices*, [Phys. Rev. B](#) **95**, 134431 (2017).
 - [45] R. Rota, F. Minganti, C. Ciuti and V. Savona, *Quantum Critical Regime in a Quadratically Driven Nonlinear Photonic Lattice*, [Phys. Rev. Lett.](#) **122**, 110405 (2019).
 - [46] A. Rubio-García, R. Molina and J. Dukelsky, *From Integrability to Chaos in Quantum Liouvillians*, [SciPost Physics Core](#) **5**, 026 (2022).

- [47] V. Savona, *Spontaneous Symmetry Breaking in a Quadratically Driven Nonlinear Photonic Lattice*, *Phys. Rev. A* **96**, 033826 (2017).
- [48] R. Di Candia, F. Minganti, K. V. Petrovnin, G. S. Paraoanu and S. Felicetti, *Critical Parametric Quantum Sensing* (2021), [arXiv:2107.04503](#).
- [49] S. Fernández-Lorenzo and D. Porras, *Quantum Sensing Close to a Dissipative Phase Transition: Symmetry Breaking and Criticality as Metrological Resources*, *Phys. Rev. A* **96**, 013817 (2017).
- [50] T. Ilias, D. Yang, S. F. Huelga and M. B. Plenio, *Criticality-Enhanced Quantum Sensing via Continuous Measurement*, *PRX Quantum* **3**, 010354 (2022).
- [51] M. Raghunandan, J. Wrachtrup and H. Weimer, *High-Density Quantum Sensing with Dissipative First Order Transitions*, *Phys. Rev. Lett.* **120**, 150501 (2018).
- [52] C. Gerry and P. Knight, *Introductory Quantum Optics* (Cambridge University Press, Cambridge, 2004).
- [53] Note that this choice is arbitrary, and in other works the cat states define the x direction of the logical Bloch sphere. This amounts to a rotation within the logical space and an exchange between bit and phase-flip errors.
- [54] E. E. Hach III and C. C. Gerry, *Generation of Mixtures of Schrödinger-cat States from a Competitive Two-Photon Process*, *Phys. Rev. A* **49**, 490 (1994).
- [55] V. Gorini, A. Kossakowski and E. C. G. Sudarshan, *Completely Positive Dynamical Semigroups of N -level Systems*, *J. Math. Phys.* **17**, 821 (1976).
- [56] V. Gorini, A. Frigerio, M. Verri, A. Kossakowski and E. C. G. Sudarshan, *Properties of Quantum Markovian Master Equations*, *Reports on Mathematical Physics* **13**, 149 (1978).
- [57] G. Lindblad, *On the Generators of Quantum Dynamical Semigroups*, *Commun. Math. Phys.* **48**, 119 (1976).
- [58] R. Blume-Kohout, H. K. Ng, D. Poulin and L. Viola, *Information-Preserving Structures: A General Framework for Quantum Zero-Error Information*, *Phys. Rev. A* **82**, 062306 (2010).
- [59] B. Buča and T. Prosen, *A Note on Symmetry Reductions of the Lindblad Equation: Transport in Constrained Open Spin Chains*, *New J. Phys.* **14**, 073007 (2012).
- [60] C. Sánchez Muñoz, A. Lara, J. Puebla and F. Nori, *Hybrid Systems for the Generation of Nonclassical Mechanical States via Quadratic Interactions*, *Phys. Rev. Lett.* **121**, 123604 (2018).
- [61] C. Sánchez Muñoz, B. Buča, J. Tindall, A. González-Tudela, D. Jaksch and D. Porras, *Symmetries and Conservation Laws in Quantum Trajectories: Dissipative Freezing*, *Phys. Rev. A* **100**, 042113 (2019).
- [62] J. Thingna and D. Manzano, *Degenerated Liouvillians and Steady-State Reduced Density Matrices*, *Chaos* **31**, 073114 (2021).
- [63] Z. Zhang, J. Tindall, J. Mur-Petit, D. Jaksch and B. Buča, *Stationary State Degeneracy of Open Quantum Systems with Non-Abelian Symmetries*, *J. Phys. A: Math. Theor.* **53**, 215304 (2020).
- [64] V. V. Albert and L. Jiang, *Symmetries and Conserved Quantities in Lindblad Master Equations*, *Phys. Rev. A* **89**, 022118 (2014).
- [65] D. A. Lidar, in *Quantum Information and Computation for Chemistry* (John Wiley & Sons, Ltd, 2014) pp. 295–354.
- [66] B. Buča, J. Tindall and D. Jaksch, *Non-Stationary Coherent Quantum Many-Body Dynamics through Dissipation*, *Nat Commun* **10**, 1730 (2019).
- [67] J. Kempe, D. Bacon, D. A. Lidar and K. B. Whaley, *Theory of Decoherence-Free Fault-Tolerant Universal Quantum Computation*, *Phys. Rev. A* **63**, 042307 (2001).
- [68] D. A. Lidar, I. L. Chuang and K. B. Whaley, *Decoherence-Free Subspaces for Quantum Computation*, *Phys. Rev. Lett.* **81**, 2594 (1998).
- [69] C. Chamberland, K. Noh, P. Arrangoiz-Arriola, E. T. Campbell, C. T. Hann, J. Iverson, H. Putterman, T. C. Bohdanowicz, S. T. Flammia, A. Keller, G. Refael, J. Preskill, L. Jiang, A. H. Safavi-Naeini, O. Painter and F. G. Brandão, *Building a Fault-Tolerant Quantum Computer Using Concatenated Cat Codes*, *PRX Quantum* **3**, 010329 (2022).
- [70] J. Guillaud and M. Mirrahimi, *Repetition Cat Qubits for Fault-Tolerant Quantum Computation*, *Phys. Rev. X* **9**, 041053 (2019).
- [71] J. Guillaud and M. Mirrahimi, *Error Rates and Resource Overheads of Repetition Cat Qubits*, *Phys. Rev. A* **103**, 042413 (2021).
- [72] L. Hu, Y. Ma, W. Cai, X. Mu, Y. Xu, W. Wang, Y. Wu, H. Wang, Y. P. Song, C.-L. Zou, S. M. Girvin, L.-M. Duan and L. Sun, *Quantum Error Correction and Universal Gate Set Operation on a Binomial Bosonic Logical Qubit*, *Nat. Phys.* **15**, 503 (2019).
- [73] F. Minganti, *Out-of-Equilibrium Phase Transitions in Nonlinear Optical Systems*, Ph.D. thesis, Université Sorbonne Paris Cité (2018).
- [74] Equivalently, under this transformation, the eigenoperators are transformed to
- $$\hat{\rho}_0^{++} \rightarrow \begin{pmatrix} z^{++} & 0 \\ 0 & 0 \end{pmatrix}, \quad \hat{\rho}_0^{--} \rightarrow \begin{pmatrix} 0 & 0 \\ 0 & z^{--} \end{pmatrix},$$
- $$\hat{\rho}_0^{+-} \rightarrow \begin{pmatrix} 0 & z^{+-} \\ 0 & 0 \end{pmatrix}, \quad \hat{\rho}_0^{-+} \rightarrow \begin{pmatrix} 0 & 0 \\ z^{-+} & 0 \end{pmatrix}.$$
- [75] F. Minganti, N. Bartolo, J. Lolli, W. Casteels and C. Ciuti, *Exact Results for Schrödinger Cats in Driven-Dissipative Systems and Their Feedback Control*, *Sci Rep* **6**, 26987 (2016).
- [76] V. Y. Mynnikov, S. O. Potashin, G. S. Sokolovskii and N. S. Averkiev, *Dissipative Phase Transition in Systems with Two-Photon Drive and Nonlinear Dissipation near the Critical Point*, *Nanomaterials* **12**, 2543 (2022).
- [77] D. Roberts and A. A. Clerk, *Driven-Dissipative Quantum Kerr Resonators: New Exact Solutions, Photon Blockade and Quantum Bistability*, *Phys. Rev. X* **10**, 021022 (2020).
- [78] We choose the overlap to quantify the resistance of critical cat because it is more numerically stable than other indicator (e.g., the fidelity). Qualitatively analogous results are found using the fidelity measure for the distance between the initial and final states.
- [79] The cat size $|\alpha|^2$ scales linearly in G [c.f. Eq. (11)], so that an exponential suppression of γ_ϕ is expected in G as well as in $|\alpha|^2$.
- [80] Z. Wang, T. Rajabzadeh, N. Lee and A. H. Safavi-Naeini, *Automated Discovery of Autonomous Quantum Error Correction Schemes*, *PRX Quantum* **3**, 020302 (2022).
- [81] W. Wyss, *Two Non-Commutative Binomial Theorems* (2017), [arXiv:1707.03861](#).
- [82] P. Blasiak, A. Horzela, K. A. Penson, A. I. Solomon and G. H. E. Duchamp, *Combinatorics and Boson Normal*

- Ordering: A Gentle Introduction*, [American Journal of Physics](#) **75**, 639 (2007).
- [83] A. Wurm and M. Berg, *Wick Calculus* (2002), [arXiv:0212061](#).
- [84] D. I. Schuster, A. Wallraff, A. Blais, L. Frunzio, R.-S. Huang, J. Majer, S. M. Girvin and R. J. Schoelkopf, *Ac Stark Shift and Dephasing of a Superconducting Qubit Strongly Coupled to a Cavity Field*, [Phys. Rev. Lett.](#) **94**, 123602 (2005).
- [85] Z. Wang, S. Shankar, Z. Mineev, P. Campagne-Ibarcq, A. Narla and M. Devoret, *Cavity Attenuators for Superconducting Qubits*, [Phys. Rev. Applied](#) **11**, 014031 (2019).